Bachelor's Thesis

Entwicklungen im Detektorkontrollsystem des ATLAS ITk

Developments in the ATLAS ITk Detector Control System

prepared by

Manuel Riedemann

from Nienburg/Weser

at the II. Physikalischen Institut

Zusammenfassung

Im Rahmen des High-Luminosity LHC-Upgrades wird der innere Detektor des ATLAS-Experiments, bestehend aus einem Pixel- und einem Streifendetektor, durch die ITk-Pixel- und ITk-Streifendetektoren ersetzt. Der neue Detektor soll die Leistung seines Vorgängers trotz erhöhter Strahlung durch die verstärkte Luminosität übertreffen. Aufgrund seiner Nähe zum Wechselwirkungspunkt sind für den Pixel-Detektor unter anderem neue Auslesechips erforderlich, um schnellere und zuverlässigere Auslesungen zu erzielen. Diese ITk-Pixeldetektormodule der nächsten Generation werden an Loaded Local Supports (LLS) in seriellen Stromversorgungsketten angeschlossen. Die beiden Arten von LLS im ITk Pixel-Detektor sind Längsträger und schräge Halbringe. Während der abschließenden Entwurfsprüfung wurde ein ITk Pixel OB-Systemtest mit einem Demonstrator durchgeführt. Das DCS überwacht und steuert sowohl den Demonstrator als auch den endgültigen Detektor. Ein verteiltes System nutzt WinCC OA für die SCADA-Funktionalität. In dieser Bachelorarbeit wird die innerhalb des ITk Pixel OB-Demonstrators durchgeführte Arbeit unter Verwendung des WinCC-Frameworks beschrieben.

Abstract

As part of the High-Luminosity LHC- upgrade, the Inner Detector of the ATLAS experiment, consisting of a Pixel Detector and a Strip Detector, will be replaced by the ITk Pixel and ITk Strip detectors. The new detector should surpass its predecessor's performance despite heightened radiation due to intensified luminosity. Due to its proximity to the interaction point, the challenging environment for the Pixel detector includes the requirement for new readout chips to achieve faster and more reliable readouts. These Next-generation ITk Pixel detector modules will be connected to Loaded Local Supports (LLS) in Serial Powering chains. In the ITk Pixel detector's Outer Barrel, the two types of LLS are longerons and inclined half rings. An ITk Pixel OB system test was carried out during the final design review phase using a demonstrator. The DCS oversees both the demonstrator and final detector's monitoring and control. A distributed system utilizes WinCC OA for SCADA functionality. This Bachelor's thesis presents the work conducted within the ITk Pixel OB demonstrator using the WinCC framework.

Contents

Contents

1 Introduction

Particle physics, a field driven by questions about the very fabric of reality, has captivated human curiosity for centuries. From the early philosophers of Greece, pondering the nature of the universe, to the modern marvels of particle accelerators like the Large Hadron Collider (LHC) [1] at CERN (Conseil Européen pour la Recherche Nucléaire), humanity has relentlessly sought to uncover the secrets of existence.

In Ancient Greece, Leucippus and Democritus conceptualized the atom, the supposed indivisible building block of matter. However, subsequent discoveries shattered this notion, revealing a complex world of subatomic particles such as electrons, protons, and neutrons. These particles, governed by the enigmatic laws of quantum mechanics and the principles of special relativity, form the basis of modern physics.

The Standard Model (SM) emerged as a comprehensive framework for the description of particles and three of the four fundamental forces [2]. A key contribution to this model came from Sheldon Glashow's 1961 paper [3], suggesting a theoretical framework that unified the electromagnetic and weak forces. In this work, he introduced the concept of a gauge theory with local $SU(2)_L \times U(1)_Y$ symmetry to describe both forces. The idea was that the weak force, which mediates particle decay, could be unified with the electromagnetic force by introducing a symmetry group. Steven Weinberg extended Glashow's framework by developing a more detailed electroweak model and introducing the concept of spontaneous symmetry breaking [4]. Abdus Salam finally contributed by clarifying and developing the Higgs mechanism within the context of gauge theories [5]. The resulting model came to be known as the Glashow-Weinberg-Salam (GWS) Theory.

Yet, despite its successes, the SM has left crucial questions unanswered, such as the prevalence of matter over antimatter [6] and the nature of dark matter [7]. To address these mysteries, physicists have been exploring theories beyond the SM, pushing the boundaries of our understanding.

CERN, established in 1954, serves as a hub for international collaboration in particle

physics. Its centrepiece, the LHC, propels particles to unprecedented energies, enabling groundbreaking experiments. Among its triumphs was the separate identification of the Higgs boson in 2012 in both the CMS [8] and the ATLAS [9] detectors, marking a pivotal moment in scientific history.

As CERN is preparing for the next phase of experimentation with the High-Luminosity LHC (HL-LHC) [10], researchers anticipate new challenges and opportunities. Upgrades to detectors, such as the ATLAS experiment with an all-silicon Inner Tracker (ITk), reflect the evolving landscape of particle physics.

In the introductory Chapters, the aim is to establish the groundwork for understanding the current challenges, particularly with respect to the technical challenges of particle tracking and the implementation of the detector control system. To achieve this goal, Chapter 2 will commence with a brief introduction to the particles of the Standard Model and their interaction with matter. Subsequently, Chapter 3 will provide fundamental knowledge essential for understanding silicon detectors before covering discussions about the Large Hadron Collider, the ATLAS experiment, the High-Luminosity Large Hadron Collider upgrade, and the new Inner Tracker in Chapter 4. Furthermore, Chapter 5 will elucidate the intricacies of the Detector Control System specifically tailored for the ATLAS experiment, followed by a discussion about the thermal performance of the used modules in Chapter 6 and an overview of my contributions to the detector control system in Chapter 7. The thesis will conclude with a summary of the work and an outlook on possible further projects.

2 The Particles of the Standard Model and their Interaction with Matter

2.1 The Standard Model

The Standard Model (SM) currently stands as our most comprehensive framework for understanding the fundamental particles and forces that govern the atomic and subatomic realms, except for gravity. This model enables highly accurate predictions and calculations. In total, it encompasses 17 types of fundamental particles. As illustrated in Fig. 2.1, elementary particles are categorized based on their spin characteristics. Particles with a spin of $S = \frac{1}{2}$ are identified as fermions, while those with spins of $S = 1$ (vector) or $S = 0$ (scalar) are classified as bosons [2].

The fermions are primarily divided into two groups: leptons and quarks. Leptons consist of six particles organized into three generations, each with increasing mass. Every generation contains one charged lepton and an associated neutrino, which has no electric charge. The charged leptons are the electron (e^-), muon (μ^-), and tau (τ^-), each carrying a charge of $-1\,\mathrm{e}$ while their corresponding neutrinos, are the electron neutrino (ν_e), the muon neutrino (ν_μ), and the tau neutrino (ν_τ). Quarks, on the other hand, are unique in that they possess a property known as colour charge. In the model of strong interactions, colour charge can manifest as either red (r), blue (b), or green (g). Individual quarks exhibit one of the three potential colours as their colour charge, whereas anti-quarks carry an anti-colour charge. Quarks are, similarly to the leptons, organized into three generations. Every generation contains an up-type and down-type quark with the primary distinction being their electric charge. Down-type quarks, which include the down (d), strange (s), and bottom (b) quarks, each carry an electric charge of $-\frac{1}{3}\,\mathrm{e}$. Conversely, the up-type quarks, comprising the up (u), charm (c), and top (t) quarks, each have a charge of $+\frac{2}{3}\,\mathrm{e}$. Each fermion is associated with an antiparticle that exhibits identical quantum numbers but possesses an opposite electric charge.

The bosons of the SM, include spin-1 vector bosons like gluons (g), photons (γ), Z bosons (Z^0), and W bosons ($W^\pm$). Notably, gluons and photons are massless, whereas W bosons have a mass of $80.377 \pm 0.012\,\text{GeV/c}^2$ [11] and Z bosons of $91.1876 \pm 0.0021\,\text{GeV/c}^2$ [11]. The boson known as the Higgs boson, is the only spin-0 boson in the SM. The respective field of the Higgs boson is responsible for imparting mass to other particles.

The interactions among particles are described through three fundamental Quantum Field Theories [2]: Quantum Electrodynamics (QED) delineates the electromagnetic interactions among charged particles. Within this framework, the photon acts as the gauge boson of the electromagnetic force, engaging with all fermions carrying electric charge. Quantum Flavordynamics (QFD) describes the weak interactions, which are fundamental to phenomena such as radioactive decay. In this context, the $W^\pm$ and Z^0 bosons serve as the gauge bosons, engaging with all fermions. Quantum Chromodynamics (QCD) describes the strong interactions that bind quarks within protons and neutrons, among other types of hadrons. The gluon, acting as the gauge boson of the strong force, exclusively interacts with quarks, as it couples solely to particles with colour charge [2].

While the electromagnetic and the weak force seem distinct at low energies experienced in everyday life, the electroweak theory unifies them as different manifestations of the same force. At energies above the unification threshold, approximately $246\,\text{GeV}$, these forces merge into a single force. Thus, if the temperature is high enough (around $10^{15}\,\text{K}$) the electromagnetic and weak forces combine to form the electroweak force. This behaviour led to the proposal of the Grand Unified Theory (GUT), which predicts the unification of the electromagnetic, weak, and strong forces in high enough energies. While many theoretical models propose the existence of this unified force, it has not been directly observed yet [12]. In order to make these intricate mathematical concepts more comprehensible, Feynman diagrams are used to visually illustrate the underlying mathematical framework of the particle interactions. Feynman diagrams of the fundamental interaction vertices are shown in Fig. 2.2 as an example.
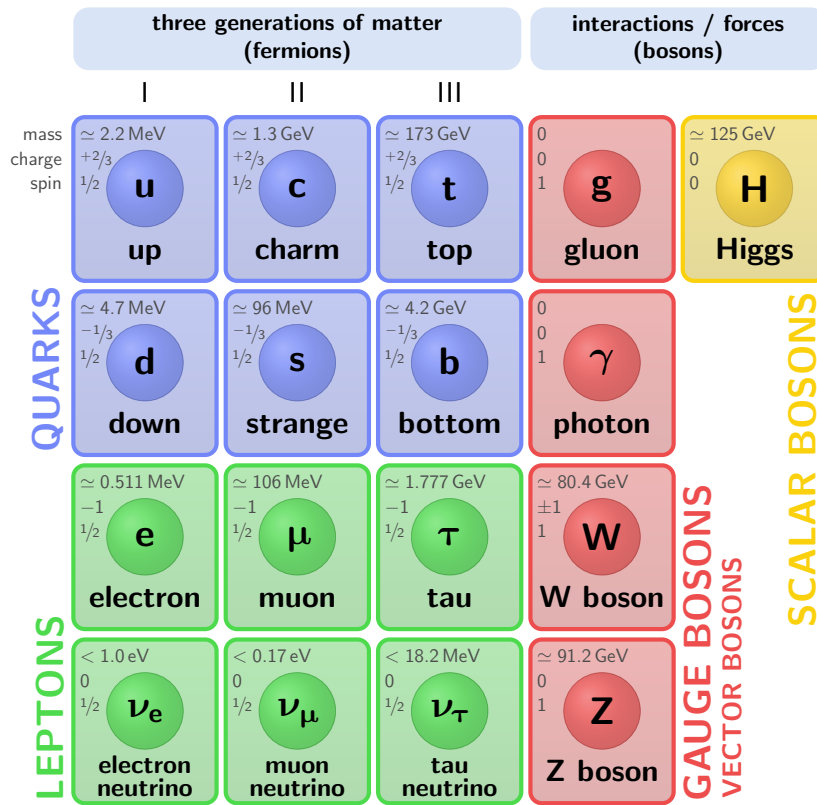
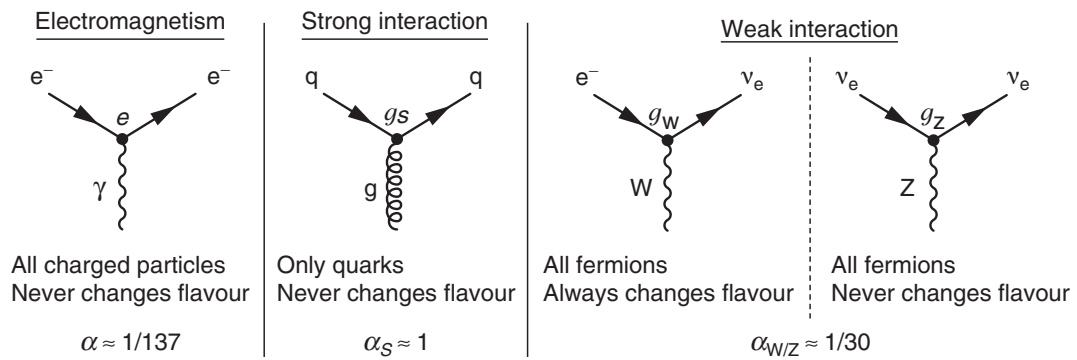Figure 2.1: Overview of the particles in the Standard Model [13].

Figure 2.2: Feynman diagrams of the fundamental interaction vertices [2].

2.2 Interactions of Particles with Matter

2.2.1 Mean Free Path of a Particle in Matter

When a particle travels through any material, there is a certain probability of it interacting with the nuclei or electrons within that material. In a very thin slice of matter, this probability is proportional to the slice's thickness and the number of potential target particles per unit volume in the material [14]. Additionally, the probability depends on the nature of the interaction. This intrinsic part of the probability is quantified by the cross-section. The cross-section is a convenient measure for discussing particle interactions in matter. When a particle passes perpendicularly through an infinitesimally thin slice of matter, the probability of interaction and the cross-section σ are related by

$$dW = dx N \sigma,$$

where dW is the probability that a particle undergoes an interaction, dx is an infinitesimal thin section of the material and N is the number of scattering centres per unit volume. The probability density function for the interaction of a particle after travelling a distance x in a medium is given by [14]

$$W(x) = e^{-xN\sigma} N\sigma.$$

The mean free path λ can then be expressed as

$$\lambda = \frac{1}{N\sigma}.$$

2.2.2 Interactions of Particles in Matter due to the Electromagnetic Force

When a charged particle penetrates a material, it interacts with the electrons and nuclei within the substance through electromagnetic forces. In a simplified model, matter can be considered as a mixture of free electrons and stationary nuclei. The charged particle is influenced by the electromagnetic fields of these electrons and nuclei, resulting in collisions with them [14].

Elastic collisions: The effects of interactions with electrons and nuclei are markedly different. During a collision with a nucleus, a charged particle loses only a minimal amount of energy but can experience a significant alteration in its trajectory, potentially even being deflected backward. Such erratic changes in the direction of a particle, as

shown in Fig. 2.3 along its trajectory, are referred to as multiple scattering [14]. For small deviation angles, this change in angle approximately follows a Gaussian distribution. The root-mean-square (r.m.s.) angular deviation of a particle traversing a thickness L, with the charge of the particle divided by the proton charge Z, the velocity of the particle v, the momentum of the particle p and the radiation length of the material X_0 is given by

$$\sqrt{<\Theta^2>} = \frac{Z}{pv}(20\text{ MeV})\sqrt{\frac{L}{X_0}}$$
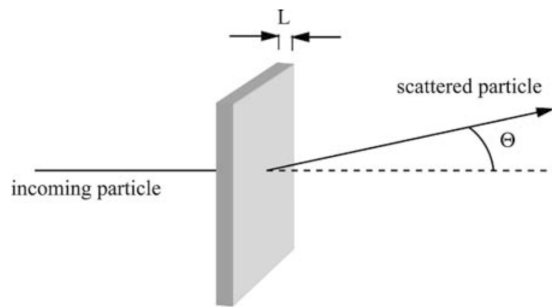

Figure 2.3: Schematic depiction of a charged particle scattering on the nuclei of the traversing material [14].

In contrast, collisions with electrons result in substantial energy transfer to the electrons, while the direction of the charged particle changes only slightly.

Inelastic collisions: As charged particles traverse matter, they can transfer their energy via inelastic collisions, creating ions that have lost their outer shell electron as well as excited atoms that have electrons in a higher energy state as their ground state. The ionisation of particles forms the basis of most particle trackers because the charge carriers (electron and ions) becoming separated is what leads to conductivity and ultimately to retraceability of the traversing particle. The degree of energy loss from inelastic collisions, suffered by a particle that traverses matter, hinges on their momentum, charge, and the nature of the target material.

In 1913, Niels Bohr made the first attempt to quantify this behaviour. The classical, non-relativistic nature of his model proved to be inaccurate, particularly for lighter particles. With the help of quantum mechanical perturbation theory, Bethe formulated the non-relativistic [15] and the relativistic Bethe formula in 1930 and 1932 respectively. For a particle with speed v, charge z, and Energy E, travelling a distance x in a material with n as the electron number density and mean excitation energy I, the energy loss of a particle per unit length travelled can be expressed by the relativistic Bethe formula

$$-\left\langle \frac{dE}{dx} \right\rangle = \frac{4\pi}{m_e c^2} \cdot \frac{nz^2}{\beta^2} \cdot \left(\frac{e^2}{4\pi\epsilon_0} \right)^2 \cdot \left[ln\left(\frac{2m_e c^2 \beta^2}{I \cdot (1-\beta^2)} \right) - \beta^2 \right]$$

where c is the speed of light, m_e the mass of the electron, e the elementary charge, $\beta = \frac{v}{c}$ and ϵ_0 the vacuum permittivity. In Bethe's theory, the material is described by a single number, the mean excitation energy I. This was questioned by Felix Bloch in 1933, who demonstrated that the mean excitation energy of atoms can be approximated [16] with

$$I = 10\,\text{eV} \cdot Z. \tag{2.1}$$

The atomic number of the atoms in the material is denoted by Z. Introducing this approximation into the given formula results in the Bethe-Bloch expression. Using an accurate table of I versus Z instead of the formula or normalizing by density ρ yields better results. This material dependency is demonstrated in Fig. 2.4.
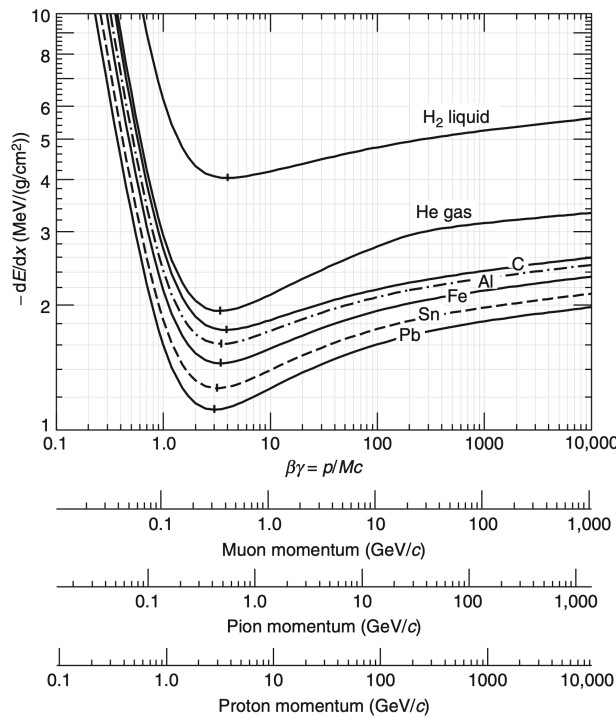
Figure 2.4: The graph of the Bethe-Bloch formula for various particles and materials [17].

Since the energy loss near the minimum is approximately the same for many radiation particles and absorber materials relevant in particle physics, particles with an energy near the minimum are often grouped together and referred to as MIPs (Minimum Ionising Particles). The ITk at ATLAS, explained in Chapter 4.5, is designed to effectively track

particles with a range from $\beta\gamma \approx 1$ (for slower, heavier particles) up to very large values, potentially exceeding several thousand (for ultra-relativistic particles).

Generalized model: At low energies, energy loss is dominated by ionisation and can therefore be predicted by the Bethe Bloch formula. However, for energies above the critical energy, radiation effects like the Bremsstrahlung dominate. The dependencies of radiation and ionisation energy loss on the particle's energy E, mass M, and nuclear charge Z of the medium differ and are given as follows:

$$\text{Ionization} \propto Z \ln \frac{E}{M}$$

$$\text{Bremsstrahlung} \propto Z^2 \frac{E}{M^2}$$

At low energies, ionisation predominates, while at higher energies, Bremsstrahlung prevails; they intersect at the critical energy E_c [18]. For tracking, ionization is the physical process that is most relevant.

$$\left(\frac{dE}{dx} E_c \right)_{\text{ion}} = \left(\frac{dE}{dx} E_c \right)_{\text{rad}} .$$

Electromagnetic radiation, known as Bremsstrahlung, is generated when a charged particle decelerates upon encountering and being deflected by another charged particle. The kinetic energy of the moving particle is converted into radiation (i.e., photons), preserving the law of conservation of energy [19].

The diagram in Figure 2.5 shows the energy loss of positive muons in copper. The vertical bands mark distinct areas representing various theoretical frameworks.

In the relevant range $\beta\gamma > 1$ for the ITk, ionizing effects dominate at energies below the critical energy $E_{\mu c}$. In this regime, the Bethe-Bloch formula is applicable. At energies above $E_{\mu c}$, radiative effects like the Bremsstrahlung become more dominant, resulting in a decadic logarithmic growth of the energy loss with increasing momentum at high energies.
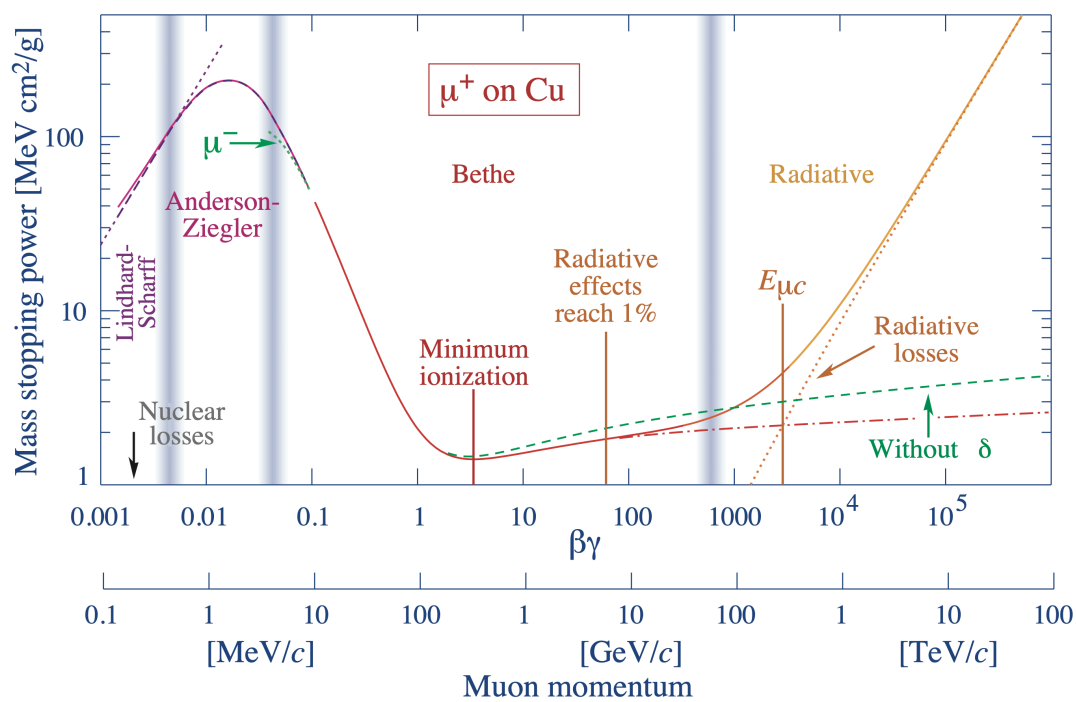
Figure 2.5: The graph of the extended Bethe-Bloch formula [11].

3 Silicon Detectors

In the ATLAS experiment at CERN, silicon detectors with high spatial resolution and radiation hardness are crucial for high-precision tracking and vertex measurements. Understanding the physics and engineering of these detectors is vital for maintaining the integrity of experimental results in high-energy physics and improving the performance and reliability of ATLAS's detector control system.

3.1 The Band Model

In quantum mechanics, electrons within atoms are confined to specific energy levels known as orbitals, which define their possible energy states. However, in solid materials, where many atoms form a tightly packed structure, these orbitals merge due to the proximity of the atoms. This merging results from the significant overlap of the wave functions of electrons in adjacent atoms, modifying their wave functions into molecular orbitals that span across multiple atoms. In a large-scale solid, this effect leads to the formation of energy bands instead of isolated energy levels [20].

These energy bands are continuous ranges where electrons can occupy various energy levels. The valence band is the highest energy band that electrons naturally occupy, playing a crucial role in bonding between atoms to form the material. Above the valence band lies the conduction band, which is essential for the material's ability to conduct electricity. This band is typically partially filled with electrons or empty, providing a path for electrons to move and carry electric current [20].

The transition from distinct, isolated energy levels in atoms to broader, continuous energy bands in materials introduces the concept of the band gap, the energy difference between the valence band's top level and the conduction band's bottom level. This gap is crucial when determining a material's electrical conductivity. Materials with a large band gap, typically greater than $2\,\mathrm{eV}$, are generally considered insulators because the energy required to excite an electron across the gap is high. This results in minimal free electrons and hence lower conductivity. Semiconductors have smaller band gaps (around $1\,\mathrm{eV}$ to $2\,\mathrm{eV}$) and exhibit varying electrical conductivity depending on the energy provided, for example

through heat or light. Conductors, on the other hand, either have minimal band gaps or none, allowing electrons to move freely and conduct electricity efficiently. Two energy levels and band gaps are shown in Fig. 3.1.
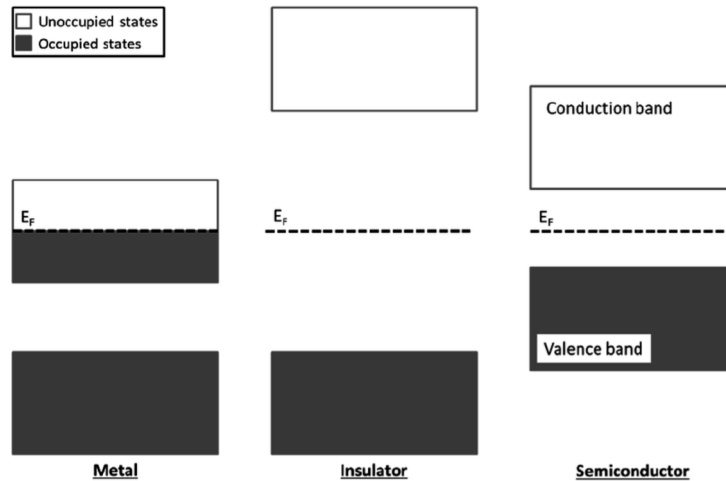

Figure 3.1: Band structure of metals, insulators, and semiconductors are shown [21]

.

3.2 Doping

By strategically inserting foreign atoms into the semiconductor's crystal structure, the electrical behaviour of the material can be adjusted. This technique, known as doping, introduces new possible energy levels for the electrons into the semiconductor. For instance, when a 5-valence element like phosphorus, arsenic, or antimony is introduced into a 4-valence semiconductor material, it leads to the creation of n-type doping. Here, the foreign atoms provide an extra electron, which is not tightly bound within the lattice. These free electrons enhance the material's conductivity [22]. In the band model, this process can be interpreted as an introduction of a donor energy level, as shown in Fig. 3.2 (left).

Conversely, p-type doping occurs when a 3-valence element such as boron or aluminium is introduced. This process creates a deficit of electrons, or 'holes', in the semiconductor's structure. These holes act like positive charges that move through the lattice, accepting electrons from neighbouring atoms, which also facilitates electrical conduction[22]. In the band model, this process can be interpreted as an introduction of an acceptor energy level as shown in Fig. 3.2 (right).
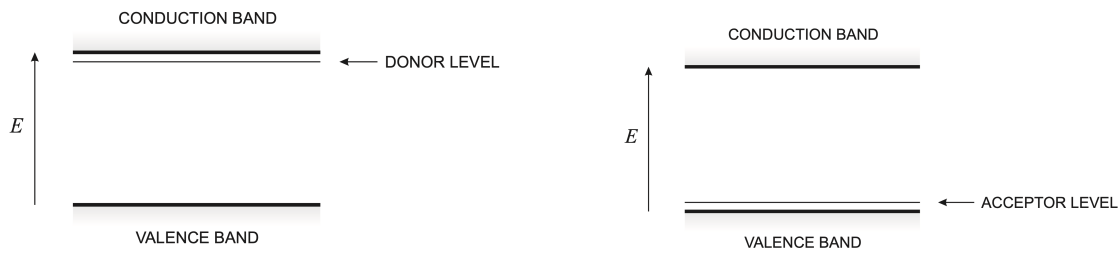
Figure 3.2: Schematic illustration of the energy band after n-doping (left) and p-doping (right) [23].

3.3 PN-Junctions

When the p-doped and n-doped semiconductors are combined, free electrons from the n-type material diffuse into the p-type material, where they recombine with holes. This diffusion of carriers (electrons and holes) across the junction results in a region devoid of free charge carriers, known as the depletion zone. The electric field in this region provides a barrier that prevents further movement of electrons and holes across the junction under equilibrium. In this state, the valence and conduction bands curve to maintain the Fermi level uniform as shown in Fig. 3.3.

When a forward bias is applied (positive voltage at the p-type side and negative at the n-type side), the width of the depletion zone narrows. In the band model, this results in a split of the Fermi-Level into two quasi-Fermi Levels E_{F_p} and E_{F_n}. E_{F_p} shifts upwards in the p-region and E_{F_n} downwards in the n-region as shown in Fig. 3.3, reducing the energy difference and therefore allowing charge carriers to cross the junction more easily [22].

Conversely, when a reverse bias is applied (negative voltage at the p-type side and positive at the n-type side), the width of the depletion zone widens. In the band model, this results in a similar split of the Fermi-Level only that E_{F_p} shifts downwards in the p-region and E_{F_n} upwards in the n-region as shown in Fig. 3.3, increasing the energy difference and therefore impeding charge carriers to cross the junction [22].

Deliberate doping or impurities can lead to exceptions which may create additional energy levels that can act as donors or acceptors, depending on their position in the band gap. Levels in the middle of the band gap can contribute as generation-recombination centres to increase the so-called detector leakage current, which corresponds to the reverse current of a pn-junction.
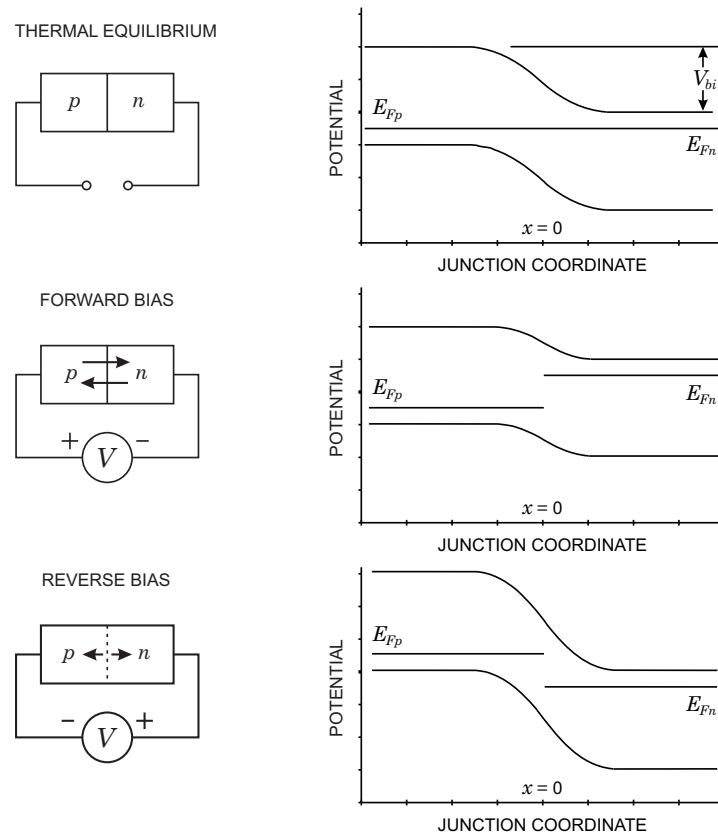
Figure 3.3: The band model of a p-n-junction is depicted with the quiescent state in the top, the forward biased state in the middle and the reverse biased state in the bottom [23].

3.4 Pixel Detectors

To track particles, pn-junctions are typically set in reverse bias, which enlarges the depletion zone, resulting in a sensitivity to charged particles. As particles move through the depletion zone, they ionize the semiconductor's atoms, displacing electrons. This ionization generates free charge carrier, which then drifts towards the electrodes due to the electric field within the depletion zone. This movement creates a detectable current pulse [18].

The main concept behind pixel detectors is to divide pn-junctions into a grid of small, square-shaped regions called pixels. Each pixel can independently detect and record the information from incoming particles.

While pixel detectors offer significant advantage in sensor technology and electronic integration over other detection types, the economic aspects pose challenges that impact

the broader adoption of such sophisticated detector systems in practical applications. Even though there are many methods of technological implementations, the two main approaches are hybrid and monolithic pixel detectors [18].

In hybrid pixel detectors, the separation of the readout electronics and the sensor into two distinct silicon chips is a strategic design choice which enhances performance and flexibility. This configuration allows for an independent optimisation of each component [18].

The connection between these two chips is typically achieved through bump bonding, which involves small metal balls that create micro-welds between the chips, or through an adhesive layer that mechanically stabilizes the connection while maintaining electrical continuity, as shown in Fig. 3.4.

The readout chip, which is separate from the sensor, can fully utilize commercial semiconductor processes. This arrangement allows for the integration of advanced electronic circuitry designed for signal processing directly adjacent to the sensor.
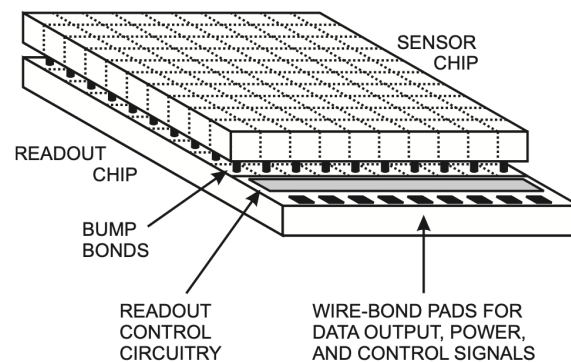

Figure 3.4: The diagram depicts a hybrid pixel detector. The pixelated sensor chip is linked to a corresponding array of readout amplifiers through a two-dimensional array of solder bumps [23].

3.5 Radiation Damage

Semiconductor detectors located near the beam pipe, such as those in the ATLAS experiment, are subject to a high particle flux and intense radiation. This radiation includes both ionising and non-ionising types. While ionising radiation is generally reversible and does not permanently damage the semiconductor material, non-ionising radiation causes more serious, irreversible harm. When high-energy particles strike the crystal lattice, the displaced atoms can dislodge additional atoms before coming to rest, creating chains of disruptions [18].

The simplest form of damage are primary point defects, where incoming particles knock the lattice atoms out of their positions. Some of these displaced atoms leave behind vacancies. Others end up in spaces between the regular lattice structures. Beyond these mechanical disruptions, the lattice may also undergo neutron captures and nuclear transmutations. Many of the primary point defects are unstable and tend to revert either by recombining with other defects or by returning to their original lattice positions. However, the inherent mobility of these defects allows them to migrate through the lattice and interact with impurities or other foreign atoms to form defect complexes. Such complexes are more stable and can permanently alter the properties of the material [18].

These stable defect complexes can significantly affect the semiconductor's electronic behaviour. For instance, they can change the concentration and types of dopants within the semiconductor material, sometimes even causing a type inversion [18].

In the case of the ITk pixel detector at ATLAS, radiation-induced damage can result in increased leakage current, reduced charge collection efficiency, and complete malfunction of pixel sensors. To ensure consistent performance over its operational lifetime, particularly with regard to the upcoming High luminosity upgrade explained in Chapter 4.4, it is essential to comprehend and counteract radiation impacts on the ITk pixel detector.

3.6 Momentum Determination in Particle Trackers

The magnetic field in the detector deflects the charge carriers, with the Lorentz force acting as the centripetal force. Therefore, we can calculate the transverse momentum via

$$\left|\vec{F}_L\right| = \left|\vec{F}_Z\right| \Leftrightarrow p_{\mathrm{T}} = qBR, \tag{3.1}$$

with the centripetal force $\vec{F}_Z$, the Lorentz force $\vec{F}_L$, the magnetic field B, the charge q, the transverse momentum p_{T} and the deflection radius R [14]. Using the Sagitta length s and the length l as illustrated in Fig. 3.5, we can apply the Pythagorean theorem to obtain:

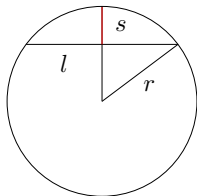$$l = 2\sqrt{2rs - s^2}. \tag{3.2}$$

Figure 3.5: Illustration of the Sagitta length

For small s, we obtain $R \approx \frac{l^2}{8s}$. Consequently, the transverse momentum can be expressed as [14]

$$p_{\mathrm{T}} = qB\frac{l^2}{8s}. \tag{3.3}$$

Using the Gaussian error propagation, the error is given by

$$\sigma_{p_{\mathrm{T}}} = \frac{p^2}{qB}\frac{\sigma_{\mathrm{mess}}}{l^2}\sqrt{\frac{720}{N+4}}, \tag{3.4}$$

where N represents the number of measurements and σ_{mess} denotes the error of the position measurement. When considering Coulomb scattering, an error of $\sigma_{p_{\mathrm{T}}}^{CS} \approx \frac{0.016\,p}{Bl}\sqrt{\sum \frac{d}{X_0}}$ with the thickness d of the traversed object and the mean radiation length X_0, must be added [14]. Therefore, we get the momentum resolution

$$\frac{\sigma_{p_{\mathrm{T}}}}{p} \approx \frac{p}{qB}\frac{\sigma_{\mathrm{mess}}}{l^2}\sqrt{\frac{720}{N+4}} + \frac{0.016}{Bl}\sqrt{\sum \frac{d}{X_0}}. \tag{3.5}$$

It is important to note that $\frac{\sigma_{p_{\mathrm{T}}}}{p} \sim p_{\mathrm{T}}$ and $\frac{\sigma_{p_{\mathrm{T}}}}{p} \sim \frac{\sigma_x}{Bl^2}$. For optimal tracking, p_{T} should therefore be minimal, and the tracker large, precise and with a strong magnetic field.

4 The LHC, ATLAS and the High-Luminosity Upgrade

4.1 The Large Hadron Collider

The Large Hadron Collider (LHC) at CERN in Geneva, Switzerland is a 27 km long synchrotron particle accelerator, designed to accelerate protons and lead nuclei, achieving a centre of mass energy of up to $\sqrt{s} = 14$ TeV [24].

Before the particles in the LHC can reach such high energies, they have to pass through a series of accelerators, as shown in Fig. 4.1. The process starts with the linear acceleration of hydrogen ions (H^-) to an energy of 160 MeV in the Linear Accelerator 4 (LINAC 4). Afterwards, the electrons of the ions are stripped away, leaving just the protons. These protons are then injected into the Proton Synchrotron Booster (PSB) where they are accelerated to 2 GeV. Next, the protons are injected into the Proton Synchrotron (PS), where their energy is increased to up to 26 GeV. The Super Proton Synchrotron (SPS) further accelerates the protons to 450 GeV. Finally, the protons are injected into the LHC where they are brought up to their maximum energy of up to 6.5 TeV [24].

In the four experiments (ATLAS, CMS, LHCb and ALICE) situated along the LHC, protons from the clockwise and counter-clockwise beam line are collided. These collisions are called events or interactions. The rate of events generated by LHC collisions is given by [24]:

$$\frac{dN_{\text{event}}}{dt} = \sigma_{\text{event}} L, \tag{4.1}$$

with the cross-section σ_{event} and the instantaneous luminosity L of the underlying event. To obtain the total number of events generated over a set time, we integrate the rate of events in Equation 4.1 over the time and obtain

$$N_{\text{event}} = \sigma_{\text{event}} \int L \, dt, \tag{4.2}$$

with the integrated luminosity $\int L \, dt$ because σ_{event} is constant in time.

The CERN accelerator complex
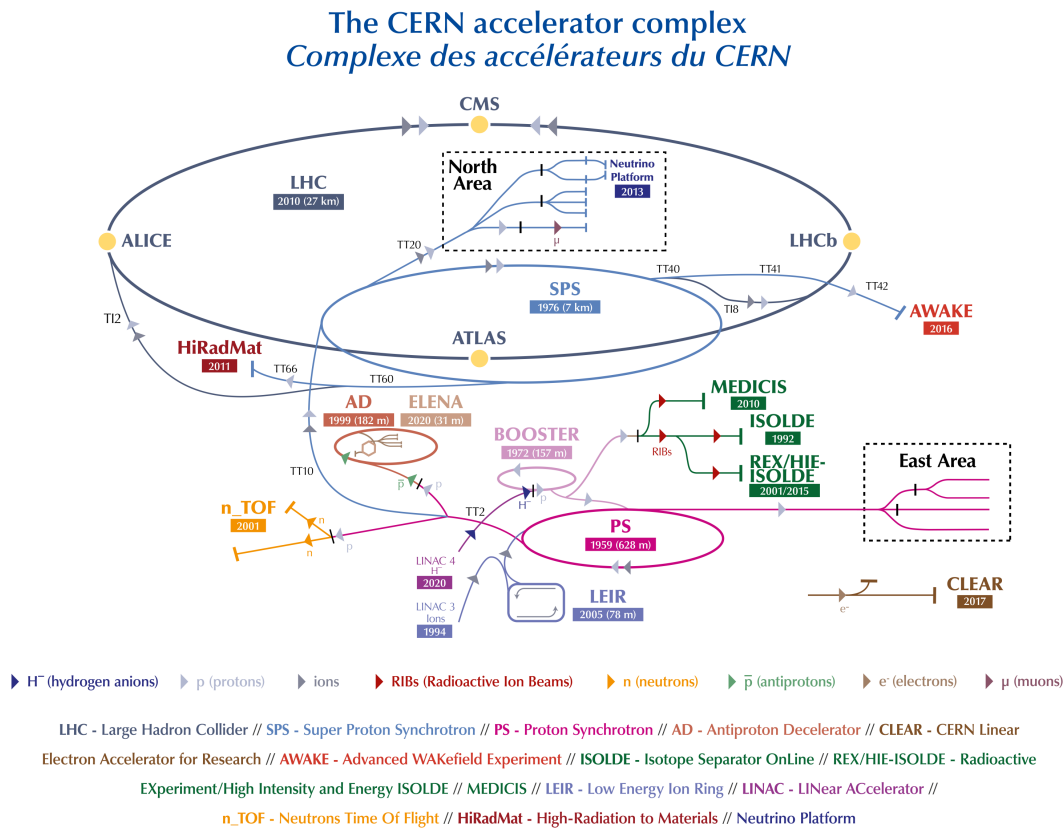*Complexe des accélérateurs du CERN*

Figure 4.1: Overview of CERN and its colliders and detectors as of 2022 [25]

4.2 The ATLAS Detector

The ATLAS (A Toroidal LHC ApparatuS) detector is a general-purpose particle physics experiment at the LHC, renowed for its substantial size, measuring $25\,\mathrm{m}$ in diameter and $44\,\mathrm{m}$ in length, with a weight of about $7 \times 10^6\,\mathrm{kg}$. The entire detector consists, of the inner detector, which will be explained in more detail in Chapter 4.3, surrounded by the electromagnetic calorimeter, followed by the hadronic calorimeter. The entire system is enclosed within the detector's outer shell, which houses the magnet system and muon spectrometer. A cutaway view of the entire detector can be seen in Fig. 4.2. Its immense scale and versatility enables ATLAS to perform a wide array of particle physics experiments in parallel to the Compact Muon Solenoid (CMS), the other general-purpose detector at the LHC [26].
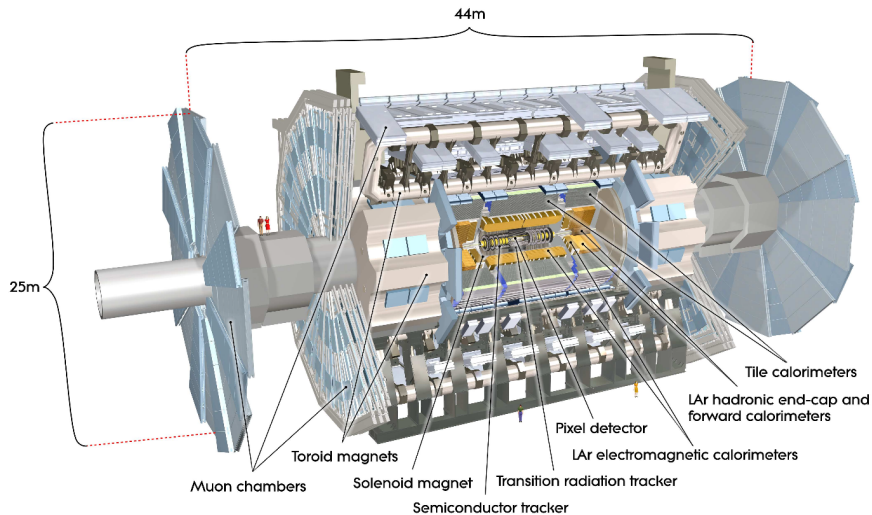
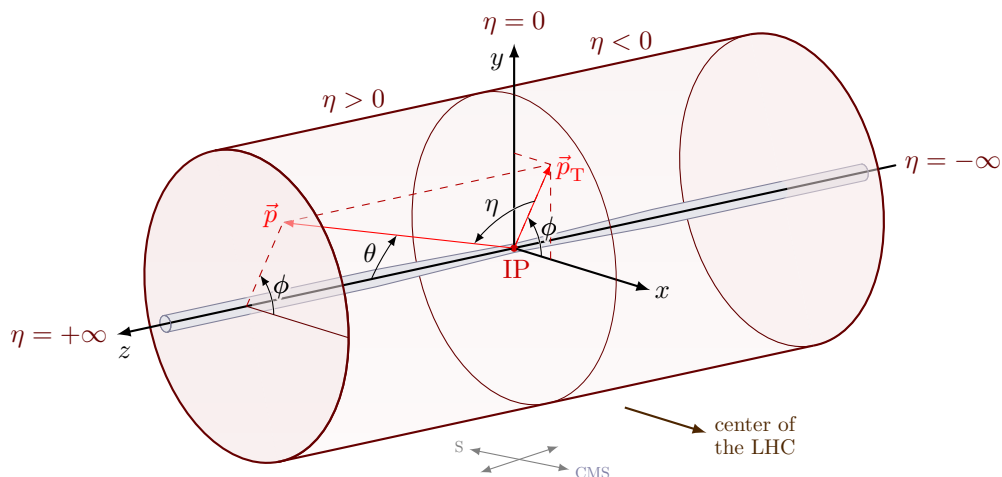Figure 4.2: Cut-away view of the entire ATLAS detector

Figure 4.3: Schematic representation of the coordinate system of the ATLAS detector

In order to construct a right-handed coordinate system in the ATLAS detector, the nominal interaction point is positioned into the origin as shown in Fig. 4.3. The z-axis aligns with the beam direction, and the x-y plane, which is perpendicular to the beam direction, has the x-axis oriented towards the centre of the accelerator ring and the y-axis pointing upwards. Because of the shape of the detector, cylindrical coordinates (r, ϕ) are often utilized, where ϕ represents the azimuthal angle around the z-axis. The rapidity y is a measure commonly used in high-energy physics, defined in terms of the energy E, the speed of light c and the longitudinal momentum p_z as:

$$y = \frac{1}{2} \ln \frac{E + p_z c}{E - p_z c}. \tag{4.3}$$

21

The pseudorapidity η on the other hand is defined in terms of the polar angle θ as

$$\eta = -\ln \tan \frac{\theta}{2} \qquad (4.4)$$

and represents the high-energy approximation ($E \approx p$) of the rapidity. Due to its simplicity and the prevalence of high-energy particles in detections, it is the parameter most commonly utilized. Furthermore, the *A*-side of the detector is designated as the region with positive z, while the *C*-side corresponds to the area with negative z. The detector's design ensures extensive coverage of the solid angle surrounding the interaction point, except for the narrow cylinder occupied by the beam pipe [26].

4.3 Inner Detector

Displayed in Figure 4.4, the layout of the Inner Detector (ID) within the ATLAS experiment encompasses the pixel detector, the semiconductor detector (SCT), and the transition radiation tracker (TRT). This intricate system fulfils essential roles in pattern recognition, momentum determination, and the precise measurement of primary and secondary vertex positions for charged particle tracks with high transverse momenta. Its overall coverage is up to $|\eta| \leq 2.5$. The inner solenoid generates a magnetic field of $B = 2\,\mathrm{T}$, enveloping the inner detector and steering charged particles along curved trajectories. By analysing the direction and curvature of these paths, valuable information about particle mass and charge can be derived, as explained in Section 3.6. Notably, the Inner Detector achieves a transverse momentum resolution of $\sigma_{p_\mathrm{T}}/p_T = 0.05\%\,p_T\,[\mathrm{GeV}] \oplus 1\%$ [27].

4.3.1 Silicon Pixel Detector

Directly around the collision point of the ATLAS detector is the pixel detector. It is comprised out of three cylindrical layers characterized by high granularity, facilitating precise pattern recognition through space-points collected by its silicon sensors. Constructed using FE-I3 chips [28], each featuring 2880 pixels and covering an active area of $0.58\,\mathrm{cm}^2$, resulting in a minimum pixel size of $50 \times 400\,\mu\mathrm{m}^2$ in the $\phi \times z$ plane. The detector can be divided into a barrel and end cap part. The barrel pixel detector surrounds the interaction point in a cylindrical or barrel-shaped configuration and consists of three layers of radii from $50.5\,\mathrm{mm}$ to $122.5\,\mathrm{mm}$. The end-cap pixel detector covers the end regions of the interaction point, perpendicular to the beam pipe, with three disks in the range $495\,\mathrm{mm} \leq |z| \leq 650\,\mathrm{mm}$ [26]. It complements the barrel detector by providing additional

coverage. In the barrel detector there are 1456 modules on 112 staves and in the end cap detector, 144 modules on 24 sectors. During the extended shutdown period from 2012 to 2014, the innermost layer of the pixel detector, spanning up to a radius of 3.3 cm, was replaced with the Insertable B-Layer (IBL). This upgrade aimed to enhance the tracking system's performance, which had deteriorated due to radiation damage [29]. Following the integration of the IBL, the Inner Detector now hosts over 92 million readout channels, constituting more than half of the ATLAS detector's total readout channels. Featuring the newer generation of readout chips, the FE-I4 [30], each with 26880 pixels, covers an active area of 3.36 cm². The IBL structure comprises 14 carbon fibre staves, each equipped with 32 FE-I4 chips.

4.3.2 Semiconductor Tracker

Positioned at intermediate distances from the collision point, the Silicon Microstrip Detectors utilize pairs of silicon strips to detect particles. Four rectangular silicon-strip sensors are grouped together in a module, with a second pair of sensors glued back-to-back at a stereo angle of 40 mrad with 4088 module's overall.

Each sensor in the barrel and end cap modules of the detector is equipped with six Application-Specific Integrated Circuits (ASICs), known as ABCD3TA. These six ASICs collectively form 768 strips, with each ASIC contributing 128 channels. The barrel sensors are rectangular, with dimensions of $63960 \times 63560\,\mu\text{m}^2$, and feature a readout strip pitch (the distance between two adjacent strips) of $80\,\mu\text{m}$. In contrast, the geometry of the end cap sensors is more complex due to being mounted on discs. Five distinct trapezoidal sensors shapes (designated W12, W21, W22, W31, and W32) are used in the end cap modules [31]. The dimensions and pitch ranges for these strips are detailed in Table 4.1. The two silicon detectors are cooled down with nitrogen (N_2) to -5 to $-10\,^\circ\text{C}$ to reduce thermal noise, preserve detector performance and protect from radiation damage [26]. It consists of four layers of radii from 299 mm to 514 mm in the barrel region and nine disks in the range of $853.8\,\text{mm} \leq |z| \leq 2720.2\,\text{mm}$ in each end-cap region. The primary role of the Semiconductor Tracker (SCT) is to maintain high spatial resolution and effective tracking across a broader area.

Sensor Type	Cut length	Outer width	Inner width	Readout strip pitch
Endcap W12	61060	55488	45735	$56.9 - 69.2$
Endcap W21	65085	66130	55734	$69.9 - 83.0$
Endcap W22	54435	74847	66152	$83.4 - 94.2$
Endcap W31	65540	64635	56475	$70.9 - 81.1$
Endcap W32	57515	71814	64653	$81.5 - 90.4$

Table 4.1: Dimensions and strip pitch of the different end cap sensors in μm [31]

4.3.3 Transition Radiation Tracker

At the end of the inner detector there is the Transition Radiation Tracker (TRT), with the barrel detector located at radii of 554 to 1082 mm and the end caps located at radii of 615 to 1106 mm and in the range of $827\,\mathrm{mm} \leq |z| \leq 2744\,\mathrm{mm}$ [26]. Together with the two end cap regions it has an acceptance range of $|\eta| < 2.0$. In the TRT, gaseous straw tubes detect the ionization of the gas ($Ar\text{-}CO_2\text{-}O_2$ and $Xe\text{-}CO_2\text{-}O_2$) from the particle as well as the transition radiation [18]. The transition radiation is emitted because the electromagnetic field associated with the charged particle has to readjust to the changing boundary conditions imposed by the different media. The intensity of the transition radiation grows with the Lorentz factor γ until it reaches the saturation value γ_s [18]. This makes the TRT especially particularly effective at identifying electrons, since they tend to have high Lorentz factors due to their small mass. Although the TRT offers lower spatial resolution compared to the other detectors, it compensates by covering a large area using fewer resources and by playing a pivotal role in particle identification.
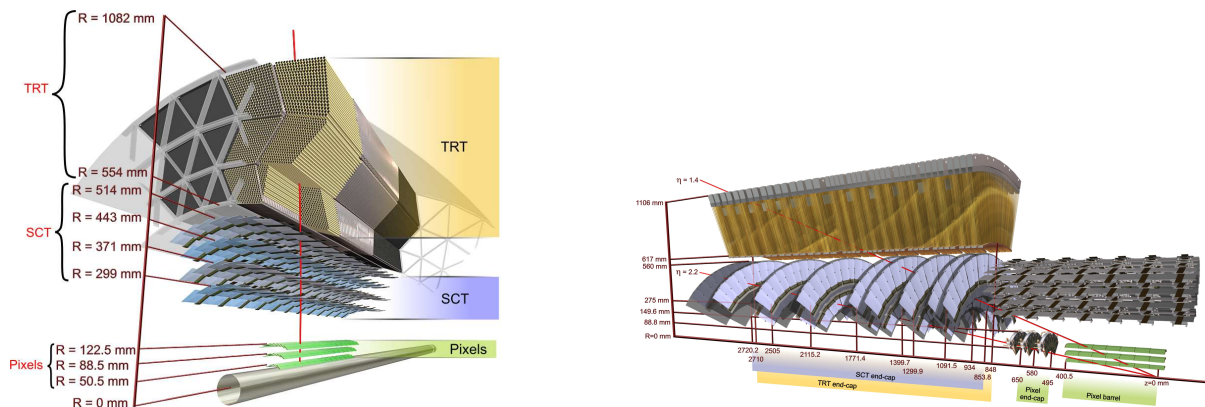

Figure 4.4: Overview of the inner detector with (right) and without (left) the end caps. A charged particle passing through the various layers and bending in the 2 T magnetic field is illustrated as a red curved line.

4.4 High-Luminosity Upgrade

The High-Luminosity Large Hadron Collider (HL-LHC) project, which is currently in development, aims to significantly enhance the capabilities of the existing Large Hadron Collider (LHC). The main goal is to increase the collider's instantaneous luminosity. This upgrade, expected to take a decade following five years of design, research, and development efforts, involves comprehensive prototyping, testing, and implementation phases. The timeline for this upgrade is shown in Fig. 4.5.

As of the end of 2025, the LHC Run 3 is scheduled to conclude the operational limits imposed by radiation damage. After some delays, the scheduled start of the third extended downtime (LS3), during which the installation of the HL-LHC will occur, is set to be in 2029. This phase will also include significant upgrades to the ATLAS and CMS detectors. These enhancements are designed not only to cope with the higher radiation levels, but also to manage the increased data volume efficiently. The HL-LHC aims for an increase of 5 to 7 times the nominal luminosity value of $10^{34}\,\mathrm{cm^{-2}\,s^{-1}}$. The HL-LHC is expected to produce more than $250\,\mathrm{fb^{-1}}$ of data per year and will be capable of collecting up to $4000\,\mathrm{fb^{-1}}$ during its exploitation period of 12 years.

This boost in luminosity will not only allow for more precise measurements of known physical processes, but also improve the chances of uncovering rare phenomena at the currently accessible energy levels. The enhanced detectors will need to at least maintain, if not exceed, their prior performance metrics to handle these new demands effectively. This ambitious project promises to push the boundaries of particle physics research, providing more profound insights into the fundamental constituents of the universe.
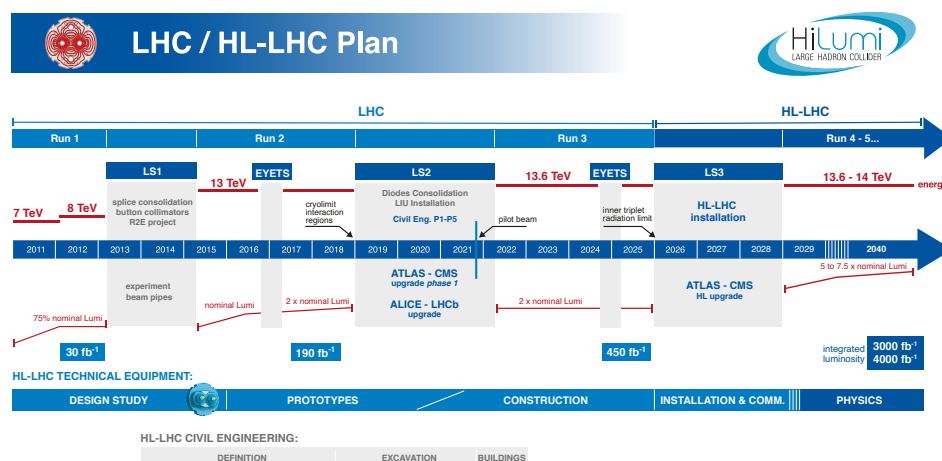

Figure 4.5: Timeline of the past and future running times of the LHC [10]

4.5 The ATLAS Inner Tracker

The forthcoming enhancement of the High-Luminosity Large Hadron Collider (HL-LHC) will substantially boost its instantaneous luminosity, presenting numerous challenges, particularly for the ATLAS sub-detectors situated near the interaction zone. Thus, the decision was made to substitute the existing Inner Detector with an all-silicon Inner Tracker (ITk).

The basic structure of the ITk will be similar to the old ID, with a Pixel Detector located at smaller radii and a large area Strip Detector surrounding it. The main difference is that the TRT will be removed due to its unsuitability for a high luminosity environment [32].

The tracking coverage is extended to a pseudorapidity of $|\eta| = 2.7$, facilitated by the strip detectors, consisting of four layers in the barrel region and six end-cap disks. Additionally, coverage is extended to a pseudorapidity of $|\eta| = 4$ through a 5-layer pixel detector as shown in Figure 4.6. The two volumes are separated by a Pixel Support Tube (PST). The active area of the silicon sensors amounts to $165 \, \mathrm{m}^2$, marking a 2.5-fold increase compared to the current ID SCT. The Pixel system incorporates roughly 10 100 hybrid pixel modules, collectively covering an active area of approximately $13 \, \mathrm{m}^2$.

A schematic depiction of the ITk layout is shown in Figure 4.6 as well as the subsystems of the Pixel detector in Figure 4.7. The inner system resides within an Inner Support Tube (IST) and is replaceable.
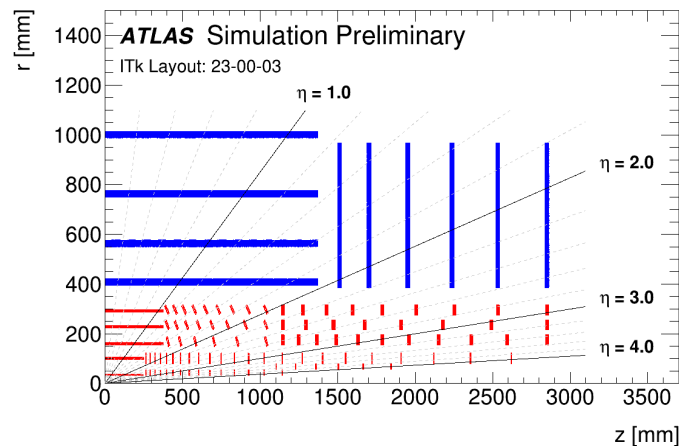

Figure 4.6: The layout of a quadrant of the ITk detector, with the strip system in blue and the pixel system in red [33].
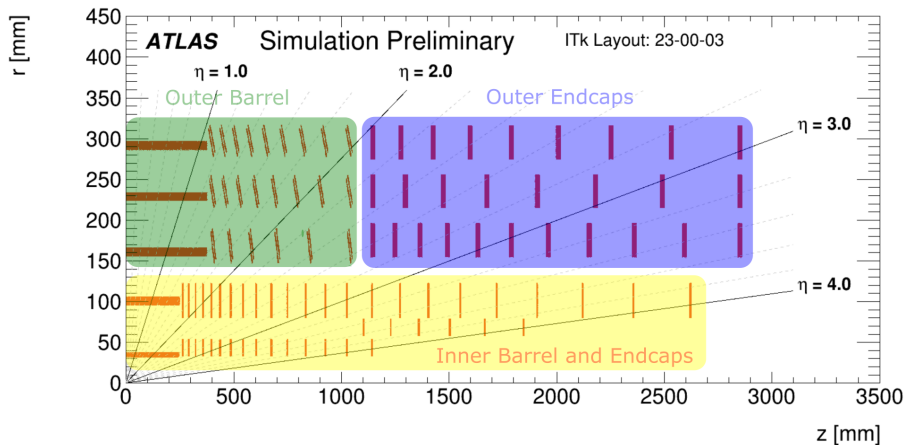
Figure 4.7: Zoomed in overview of the pixel system, delineating three regions: the Outer Barrel in green, the Outer Endcaps in blue, and the Inner Barrel with Endcaps in yellow (bottom) [33].

4.5.1 The ITk Pixel OB Demonstrator

To facilitate the progress and to test the on-detector components on all three regions of the pixel detector, system tests are planned. To conduct these tests, demonstrators of these subsystems were constructed. Each demonstrator must fulfil the technical requirements specified in Ref. [34]. Some additional requirements for the OB demonstrator are specified in Ref. [35].

Similar to the final detector, the Outer Barrel demonstrator is built out of high thermal performance carbon-composite loaded local supports structures (LLS) where the modules are mounted together with a cooling pipe. The modules are arranged in Serial Powering (SP) Chains, powered by a single current source. SP chains reduce material and cables but pose a challenge due to constant current requirement and chain failure risk if a single module fails. The sensors are biased with up to 200 V high voltage (HV) and the modules operated at 1.2 V low voltage (LV).

There are two types of LLS in the barrel region. The longerons as shown in Fig. 4.8 have four SP chains symmetric to the interaction point, and the inclined half ring as shown in Fig. 4.9 that has two SP chains with 8, 11, or 14 modules in layers 2, 3, or 4 respectively that are alternately soldered on the front and back sides of the cooling pipe for double-sided cooling. A picture of prototypes from both these support structures can be seen in Fig. 4.10.
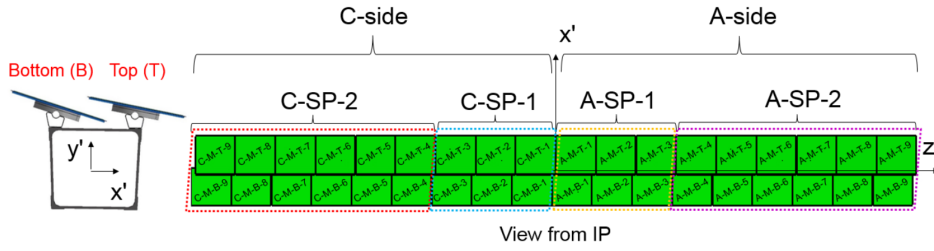
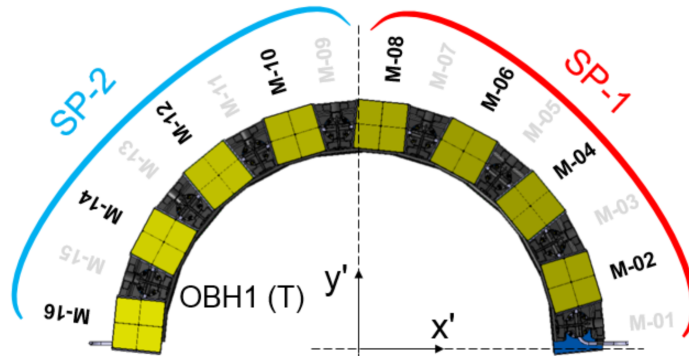Figure 4.8: Schematic overview of the longeron LLS

Figure 4.9: Schematic overview of the half rings LLS
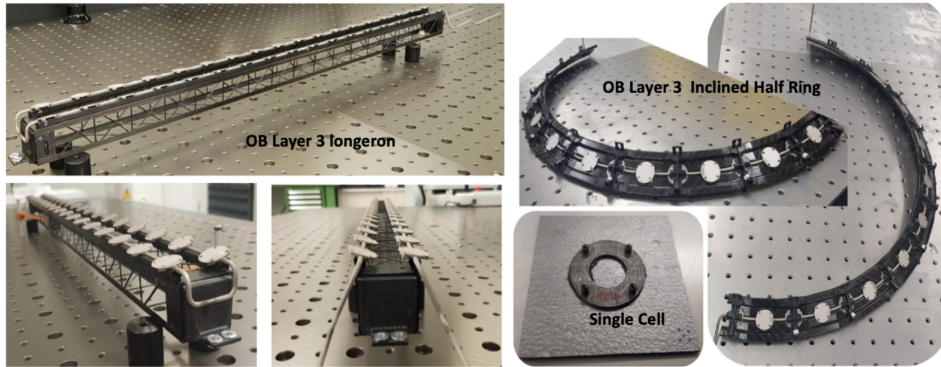

Figure 4.10: Picture of the LLS prototypes of layer 3 [36].

In the final design review, the Outer Barrel (OB) demonstrator is equipped with modules featuring the RD53A front-end chips [37]. The RD53A chip was specifically designed for testing purposes in the development of the Inner Tracker (ITk) Pixel detector and is not meant for the final experiment. These RD53A modules are half-sized demonstrator modules used to evaluate three different analog front ends and two readout architectures. From extensive testing of these RD53A modules, the ITkPixV1 modules [38] were developed for the final experiment, although they are not yet ready for system tests.

5 The Detector Control System for ATLAS

In order to manage the complex array of detector elements, totalling millions of electronic channels, a robust Detector Control System (DCS) is necessary. This system must ensure safe and coherent operation of ATLAS, serving as a unified interface for all sub-detectors and technical infrastructure. It regulates operational states, monitors parameters, detects anomalies, and facilitates communication between the detector and other systems like the LHC accelerator and CERN services [39].

The ATLAS experiment operates through two collaborative systems: The Detector Control System (DCS) and the Trigger and Data-Acquisition (TDAQ) system. The DCS oversees the experiment's hardware and infrastructure continuously, while the TDAQ system handles the readout of generated data.

The DCS architecture, illustrated in figure 5.1, is structured into Front-End (FE) equipment and Back-End (BE) systems.

The FE equipment predominantly consists of devices such as power supplies and sensors. Commercial systems are predominantly favoured for FE equipment to ensure long-term maintainability and streamlined development. Custom designs are only pursued when commercial solutions fall short of requirements. The Embedded Local Monitor Board (ELMB) serves as a multipurpose I/O device.

The BE systems, on the other hand, consist of industrial rack-mounted PCs running a distributed system of SIMATIC WinCC Open Architecture (WinCC OA) instances. WinCC OA projects are organised under respective sub-detectors, each possessing operational autonomy. To guarantee operational safety, a hardware interlock system enables independent detector shutdown in emergencies. Communication between FE and BE primarily occurs via CAN with the CANopen protocol or Ethernet with the OPC-UA protocol. The Joint Controls Project (JCOP) was established to optimize DCS efficiency across LHC experiments, establishing standards and utilising a common software package [40].
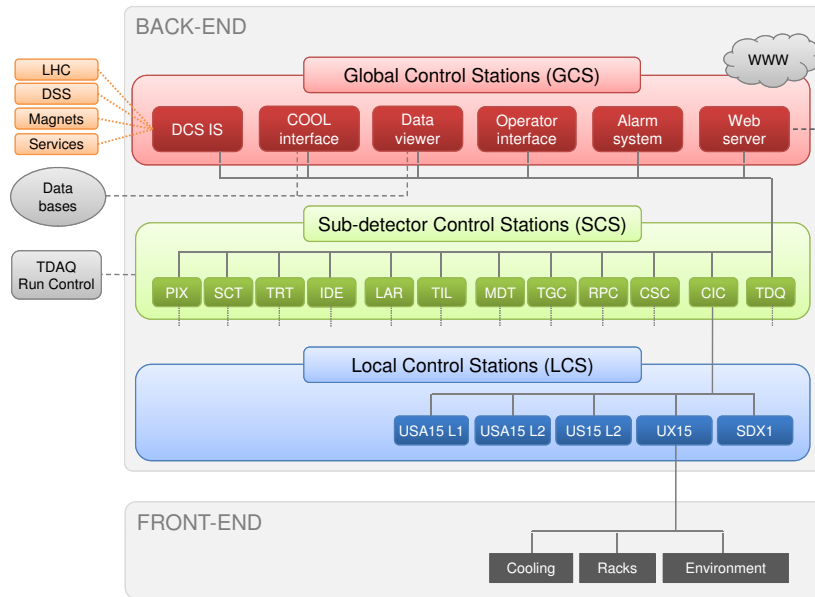
Figure 5.1: Schematic overview of the ATLAS DCS architecture [39]

In order to gain a better understanding, some components of the DCS are explained in turn below.

5.1 Hardware

ELMB: The Embedded local monitoring board (ELMB) comprises an 8-bit microcontroller managing 64 analogue inputs. A 16-bit ADC reads temperature, humidity, and dew point sensor inputs for ELMB [39]. It supports 16 digital outputs and 16 digital inputs, granting extensive functionality. The ELMB's components are chosen for their ability to function optimally in strong magnetic fields and heavy radiation.

Optoboxes: The Optoboxes house Optoboards that provide optical-to-electrical signal conversion for the SP chains in the Pixel detector. Each Optobox serves a particular SP chain, meaning that all Optoboards in an Optobox are associated with the same SP chain and are controlled as a single unit. This collective control simplifies the power distribution and monitoring, ensuring that the entire SP chain operates in sync and that the state of each component within the Optobox is monitored accurately.

Interlock: Although DCS software provides solutions for slow detector control, a hard-wired interlock system handles almost all situations where safety is an issue [41]. The interlock system is not connected to the main control system and can independently shut off required power supplies. Temperature sensors feed data directly into the interlock

system, which an FPGA uses to evaluate conditions and trigger alerts. Despite being a purely hardware-based interlock system, communication with the DCS about the interlock actions is essential. ELMBs are responsible for interlock signal monitoring. Digital output channels can be used to transmit test signals to the interlock system. The FPGA's decision-making remains unaltered.

Power supplies: ATLAS employs commercial VME (a bus system enabling communication between multiple modules) crates with integrated power supplies, stationed in radiation-free areas. Power is required for both the ELMBs and the detector electronics. Power supplies must offer over-voltage and over-current protection. The DCS manages the power supplies. The OPC-UA protocol is widely used as an interface.

Cooling system: Currently, the IBL CO_2 cooling plant is used in the OB demonstrator in SR1. The cooling loop flow can reach a maximum rate of $14\,\mathrm{g/s}$ and can function in the temperature range from $-35\,^{\circ}\mathrm{C}$ to $+20\,^{\circ}\mathrm{C}$ [42]. The operational parameters, which are communicated via DIP (a CERN Data Interchange Protocol), are imported into WinCC OA as data points using a JCOP component.

5.2 Protocols and Server

CANopen: The Controller Area Network (CAN) functions as a serial bus without requiring a designated master node. In message-based protocols, data transmission occurs sequentially. Each device is assigned a unique node ID to allow it to transmit and receive data. Lower-priority devices yield higher-priority ones on the bus [43]. CANopen5 is a protocol layer built upon CAN (Controller Area Network). The ELMB software adheres to the CANopen DS-401 Device Profile for I/O modules. The bus signal is transmitted over a twisted pair of wires. CAN offer cost savings, material savings, and resistance to magnetic fields, making it the preferred method for reading slow monitoring data from detector components.

OPC-UA: The Open Platform Communications protocol has evolved into OPC-UA. It enables complex data transfer between dispersed industrial automation systems. The new protocol version operates as an independent binary TCP/IP protocol [44]. OPC-UA facilitates comprehensive modelling and description of shared data. A client can request particular data components from a data model for exploration purposes. The client can either poll data from the server or subscribe to real-time data changes. The client and server can independently detect connection failures. Because it uses Ethernet connections, it is not usable in environments with strong magnetic fields. However, it has been selected as the standard of middleware [45].

OPC-UA servers: An efficient version of OPC-UA servers, known as the quasar framework, is accessible [46]. The quasar framework generates an executable OPC-UA server application based on the target system or device's object-oriented information model, described in its XML server design file. The OPC-UA server can be located off-site and connected to the target system via CAN or SNMP. Additionally, the server can process raw data into physical values. The OPC-UA client can only interact with the data sources specified in the server's runtime configuration file. Fig. 5.2 demonstrates the use of this method. The server connects the Wiener power supply to the SCADA system. Power supplies are commonly linked via Ethernet and SNMP protocol.
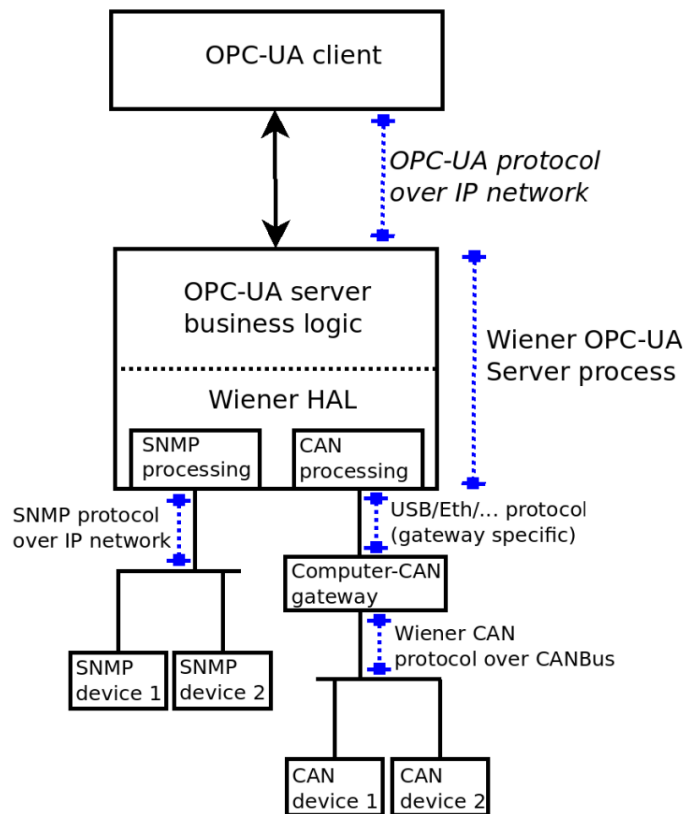

Figure 5.2: OPC-UA server in a control chain [47]

5.3 WinCC OA

Following a thorough market analysis of Supervisory Controls and Data Acquisition (SCADA) systems, WinCC OA by ETM1 emerged as the preferred choice due to its remarkable performance and scalability. The system, being an Open Architecture, offers a C++ application programming interface (API) for seamless integration of custom software. This interoperability is facilitated through the DIP and Distributed Informa-

tion Management System (DIM) software components. The system is designed to work across multiple computers, making it highly scalable and efficient. It manages real-time data as "data point elements" within a database, handling changes through event-based operations that use multiple threads for faster processing. The structure includes various managers that facilitate this distribution, enabling projects on different machines to interact smoothly. The illustration in Fig. 5.3 shows how a WinCC OA project can be organized. Communication with hardware is handled by drivers (D), while the Event Manager (EV) processes all current process variables, keeping them in memory and coordinating with other managers. The EV also manages alerts, and the Database Manager (DB) manages data storage, including configurations and historical data queries.

The essential managers to every WinCC OA project are the Database Manager and Event Manager, with other processes added as needed. The system includes Gedi, a development environment for creating scripts and panels. The scripts use a C-like language called "Control++", and panels help visualize data for better control and monitoring. The Para program provides a user interface that displays data points in an organized manner, similar to classes.

The JCOP framework enriches the development environment with tools for access control, alarm management, trending, and database configurations. It includes OPC-UA servers that connect various power sources to the system and software for managing Finite State Machines (FSMs). These FSMs are crucial for automating control tasks in complex settings like the ATLAS experiment, helping operators manage the control room effectively.
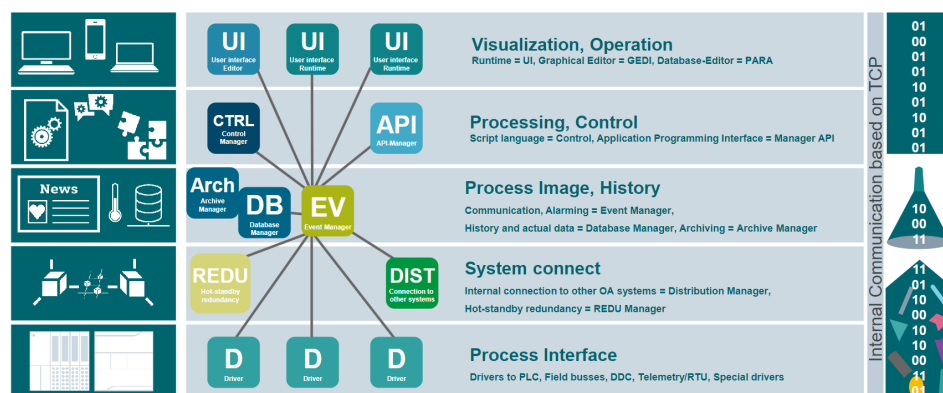

Figure 5.3: Architecture of a WinCC OA project [48]

5.4 Finite State Machines

A Finite State Machine (FSM) is a mathematical model employed to define the behaviour of an object based on its current state. As an abstract machine, an FSM exists in one of a finite number of states at any given time [49]. It transitions from one state to another in response to an input, which could be an external action or a condition being fulfilled. Graphically, this can be represented by a directed graph called a state diagram. A simplified version of the state diagram for the FSM of an SP chain in the Outer Barrel is shown in Fig. 5.4 as an example.

One of the principal advantages of FSMs is their capacity to simplify complex systems and automate decision-making processes. This attribute significantly aids in enabling non-experts to manage and operate large-scale systems efficiently. For instance, in high-stakes environments such as those in which the ITk (Inner Tracker) operates, FSMs enable operators to monitor, diagnose, and control complex hardware and software states seamlessly. By systematically managing the operational states of ITk components, FSMs reduce the potential for human error, allowing for a controlled, reliable response to conditions such as faults, reconfigurations, and adjustments in real time.
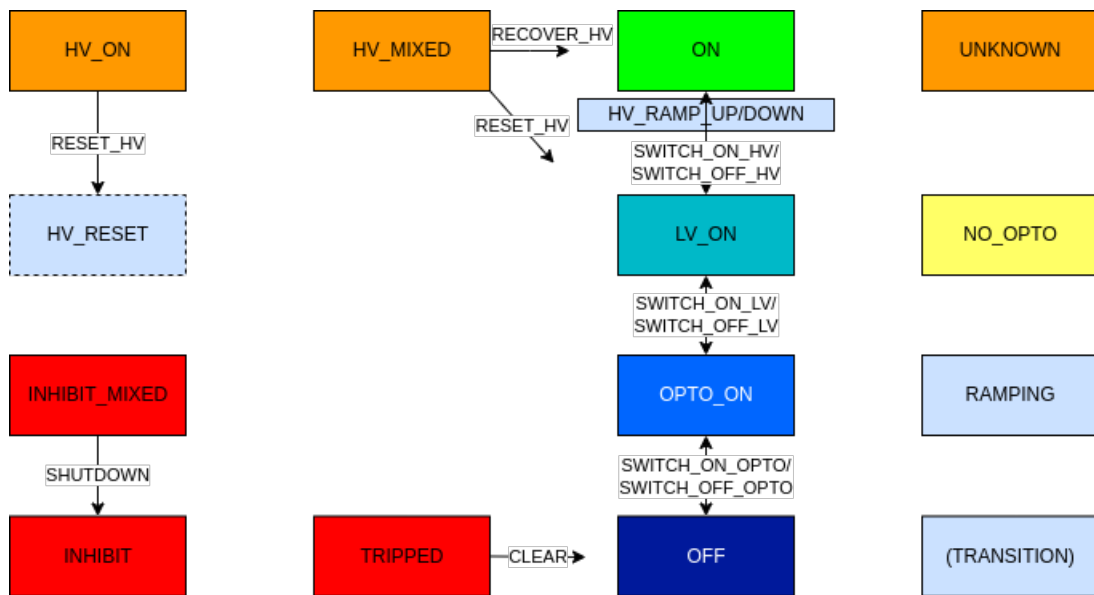
Figure 5.4: State diagram of the simplified FSM of one SP chain in the outer barrel

5.5 DCS of the ITk Pixel OB Demonstrator

For the effective system testing of the OB demonstrator, a robust control system is essential, both the requirements of the ATLAS DCS [39] and the DCS requirements for the HL-LHC [50] need to be taken into account. Utilizing an extensive Detector Control System (DCS) streamlines the workflow, allowing the operator to focus on the tests. Early use of the DCS offers valuable insights into critical functionalities needed for the final control system, even if requirements differ slightly. The demonstrator DCS features three independent communication paths with varying availability, reliability, and granularity:

- **Diagnostics:** High granularity data from each front-end chip requires the data acquisition system to be running. Each FE chip utilizes an analogue-to-digital converter (ADC) to gather various types of monitoring data, including critical temperature information. This collected data is transmitted through the standard physics data path to the Front-End LInk eXchange (FELIX) system. FELIX serves as an interface, ensuring that the monitoring data is separated from the primary data stream and then forwarded to the DCS.

- **Control and Feedback:** This path is crucial for managing the power supplies for the SP chains and Opto Boxes. Operating in a serial powering configuration means that the entire SP chain is controlled as a single unit. This path includes a detailed connection scheme for the SP chain, where one low-voltage (LV) channel from a current source powers the front-end (FE) chips, and two to four high-voltage (HV) channels are used for sensor depletion. Inside each Opto Box, all associated Opto Boards for a specific SP chain are controlled collectively. To monitor temperatures and voltages within the SP chains and Opto Boxes, the DCS interfaces with the Monitoring Of Pixel System (MOPS). MOPS is an Application-Specific Integrated Circuit (ASIC) developed for the Pixel detector [51], which aggregates on-detector monitoring data. Each SP chain is assigned one MOPS chip, which communicates with external systems via a CAN bus. The data collected by MOPS is received at PP3 (patch panel 3) by the MOPSHUB, which then forwards it to the control room. Every MOPS-HUB can simultaneously interface up to 16 CAN buses, each supporting up to 4 MOPS nodes. Notably, the MOPSHUB is powered independently of MOPS. It is crucial that the Control and Feedback path is functional for the Finite State Machine (FSM) to accurately determine the state of the Pixel detector.

- **Safety:** The hardware interlock system is designed to protect both the detector and personnel from potential hazards. This system demands the highest level of

reliability and operates continuously. To safeguard the detector from overheating, temperature sensors are installed on each SP chain and within the Opto Boxes. These sensors are crucial for monitoring temperature levels and are directly connected to the interlock system [52].

The ITk Pixel Demonstrator DCS architecture and its components are illustrated in Fig. 5.5. A dedicated DCS PC, running the WinCC OA project originally on CentOS and now on AlmaLinux, controls and monitors the demonstrator.
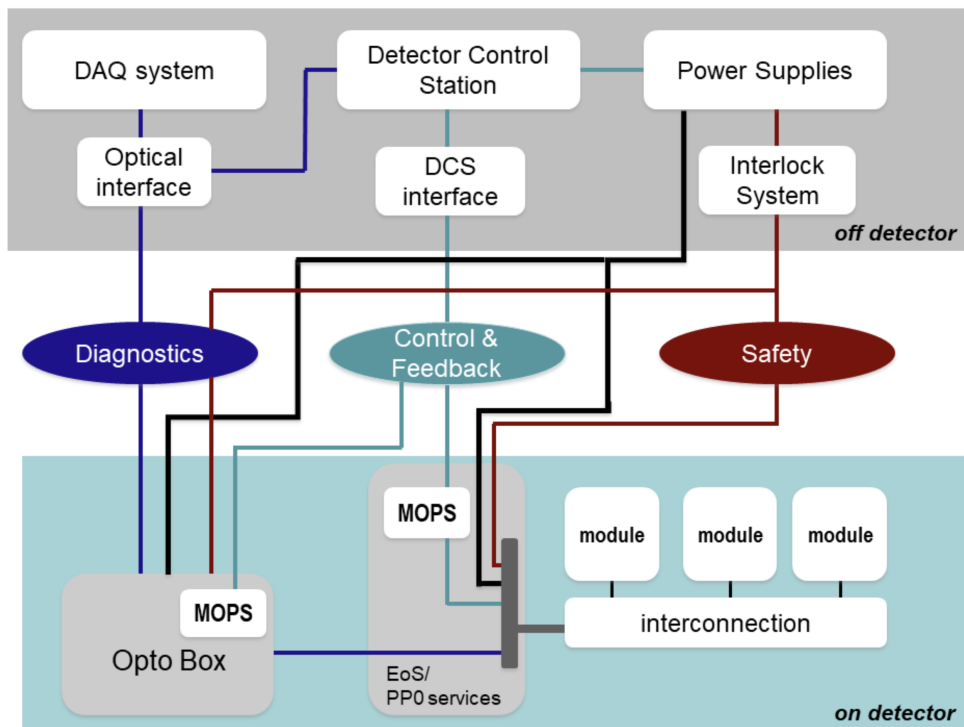

Figure 5.5: Illustration of the three different communication paths of the ITk Pixel DCS [53].

6 Thermal performance of the ATLAS ITK-Pixel Modules in the Outer Barrel

To prevent thermal damage to low-mass detector structures, the combined heat from the sensor and on-detector electronics must be cooled down during operation. This issue is further complicated by the strong temperature dependence of the sensor leakage current $I \propto T^2 e^T$ [54] and resulting leakage power, which in turn affects the temperature. Additionally, the leakage current will rise because of its direct proportionality to the fluence [55]. Reaching thermal instability if the heat generated in the detector exceeds the cooling capacity of the system must be considered a realistic scenario [54]. To effectively predict and relate critical operational parameters such as coolant temperature and radiation-induced power, a comprehensive understanding of the effectiveness of heat dissipation is therefore crucial. Despite noteworthy effort towards analytical predictions [54], the further discussion will focus on a numerical one.

The LLS structures for the three ITk Pixel detector sub-systems are built out of Carbon-fibre-reinforced polymers (CFRP) that possess low thermal expansion, excellent tensile properties, high thermal and electrical conductivities, and are strong and light materials, making them suitable for reliable support of pixel modules and a low thermal-impedance pathway to the coolant, reducing total radiation length [56].

OB local support is implemented using a modular approach. In the OB approach, module cells are manufactured separately and are attached to a framework at the end of production for easy replacement. The design of the OB module-cell, illustrated in Fig. 6.1, permits absolute re-workability at the cost of extra production steps during sub-system integration. The pixel module, which is attached to a pyrolytic graphite tile and affixed to a cooling block, is secured to a base block using screws. The base block is fastened beforehand to the local support using the attached cooling pipe as a guide. The carbon structure of the local supports encompasses the cooling pipes. Longerons connect the half rings in the inclined sections.
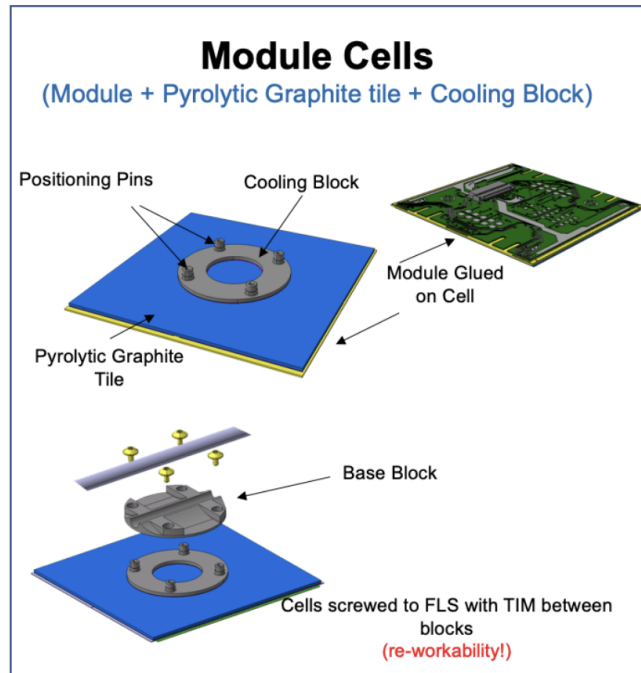
Figure 6.1: Expanded view of the Modules in the outer barrel [57]

Before production commences, local support designs undergo both qualification and validation processes. Studies employing Finite Element Analysis and prototype measurements were conducted to attain the desired result. Finite element analysis (FEA) simulates any given physical phenomenon using the numerical technique called the Finite Element Method (FEM). The finite element method is employed in engineering and mathematical modelling to numerically resolve differential equations with two or three space variables, including boundary value problems.

The detector's materials, interfaces, and assemblies must meet the specified conditions for thermal and mechanical stress, radiation damage in the final design. Experts from the three pixel detector subsystems collaborated to develop parallel and comparable thermal and mechanical models for FEA studies. The model used to reflect the structural, material, geometry and assembly characteristics of the outer barrel modules are shown in Fig. 6.2. The cooling pipe's path to the module passes through the pipe wall, base block's solder, thermal interface, cooling block, and pyrolytic graphite tile's adhesive. The FEA outcomes presented correspond to the detector's anticipated end of life, marked by maximum heat dissipation. The variability of radiation exposure in various parts of the detectors was taken into account.
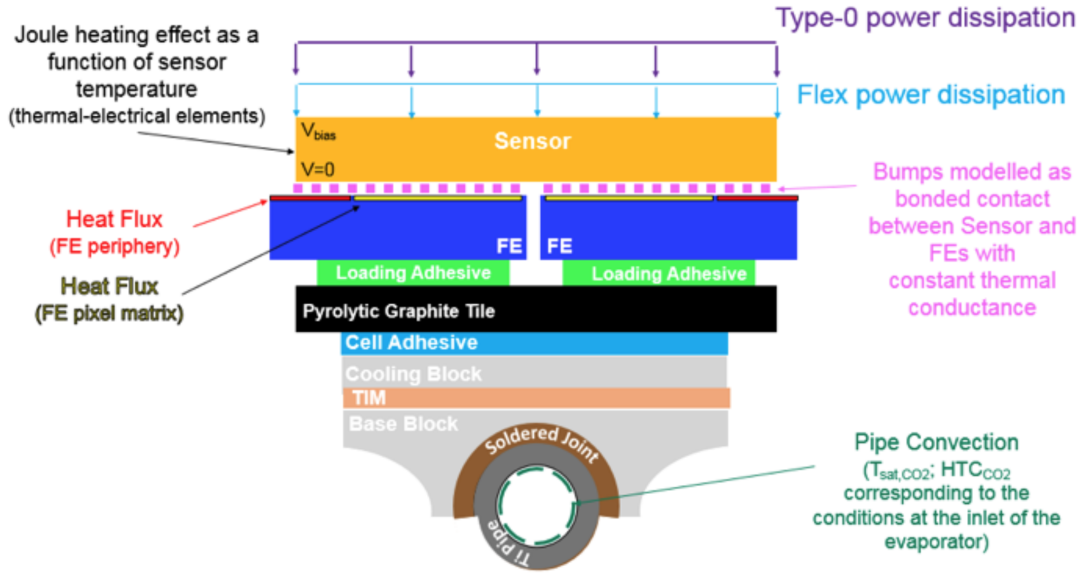
Figure 6.2: FEA of the Modules in the outer Barrel [57]

In the matrix, the sensor elements (pixels) are located. Particle detection and measurement take place here. The outer regions of the chip, also known as the periphery, surround the matrix. The signal processing, data readout, and other essential electronics for the matrix are usually located in this region. In the periphery the power dissipation is normally higher due to the presence of a multitude of active electronic components such as amplifiers, analogue-to-digital converters, and control logic. Among the many considered powering scenarios, the heat dissipation of two scenarios is compared in Table 6.1. Case 1 simulates homogeneous power dissipation in the front-end chip through the use of silicon heaters prior to real module's availability. The case was employed to authenticate the varying material properties incorporated into the model. In case 2, the power density at the FE periphery is set to be 14 times greater than the one in the pixel matrix, making it a more realistic model [57]. A visualisation of the results are shown in 6.3.

Case 1		Case 2	
Matrix	Periphery	Matrix	Periphery
0.548	0.548	0.264	3.592

Table 6.1: Expected frontend chip power dissipation in W/cm^2 with homogenous heating (case 1) and during detector operation (case 2) [57].
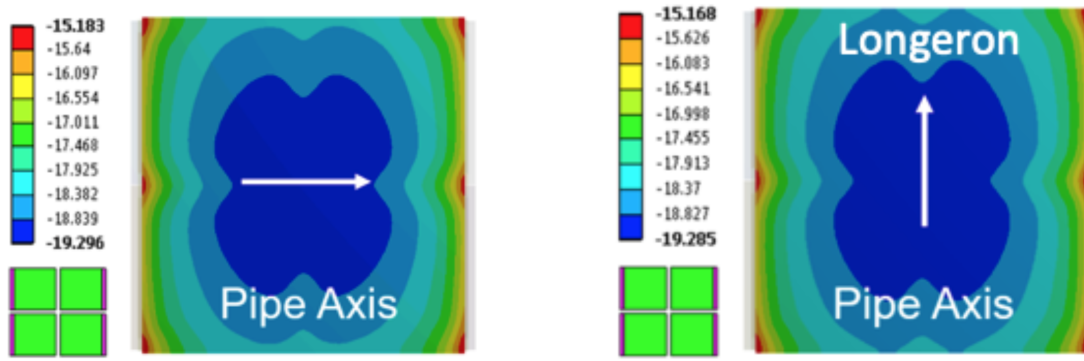
Figure 6.3: FEA results of the half ring prototype (left) and the longeron prototype (right) [57].

The Thermal Figure of Merit (TFM) represents the thermal impedance between the coolant and the hottest point on the surface of a loaded local support. It is defined as

$$TFM = \frac{T_{Max} - T_{Min}}{\frac{power}{area}}.$$ (6.1)

The FEA-calculated TFM value with $TFM_{FMA} = 24.34\,\text{K}\cdot\text{cm}^2/\text{W}$ turns out to be close to the nominal value of $TFM_{nom} = 28.85\,\text{Kcm}^2/\text{W}$ that was given by project specifications [57].

Along with FEA calculations, actual TFM measurements were taken using silicon heaters instead of the real modules (case 1). The inclined half ring and longeron meet the required specifications, as evidenced by the TFM results 6.4 where the majority of cells fall below the target value and all of them are significantly under the design value for both local supports.
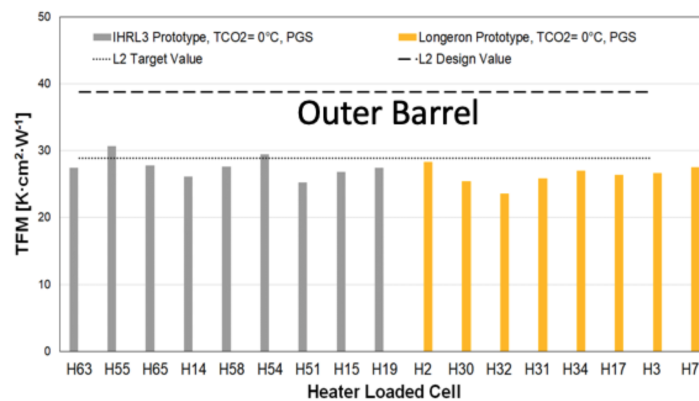

Figure 6.4: TFM measurement results for the half ring (grey) and longeron (yellow) prototypes [57]

7 Contributions to the DCS

In addition to controlling detectors, the DCS is also responsible for monitoring them. Manual monitoring, in combination with interlock safety measures, can predict errors and diagnose them. The final version of the ITk pixel detector will have a multitude of sensors that require monitoring. Table 7.1 details the number and types of environmental sensors used in the ITk volume [58]. Each module will have a temperature and voltage measure, which significantly increases the total amount of sensors. In SR1, the OB demonstrator utilizes 27 $RD53A$ modules linked in SP chains, while considering the scalability of the DCS monitoring. The environmental sensors for humidity, pressure, and dew point are sensors of the surrounding environment of the demonstrator, not the demonstrator itself. Sensors for gas flow, radiation, vibration, and strain gauges are currently absent in the single longeron system. A well-integrated display of these monitoring values in the user interface (UI) is crucial for allowing users to continuously supervise the state of the system. This ensures smooth operation of the detector and enables timely intervention in case of hardware failures.

Sensor type	Number of sensors
Temperature	1000
Humidity	30
Radiation	20
Vibration	6
Pressure	200
Gas flow	20
Strain gauges	40

Table 7.1: Planned amount of environmental sensors in the ITk project [58].

7.1 Previous Status of the Monitoring Software

As part of this Bachelor's thesis, new aspects of the manual monitoring of single modules were implemented into already designed and programmed panels.

The previous design of the monitoring panels, shown in Fig. 7.2 and Fig. 7.3, were created during the Master's thesis work of Anne Gaa [59]. The development focused on singly LLS panels, which included temperature and voltage difference data for each module. The voltage difference corresponds to the difference between a module's voltage to that of the next one. LLS chains are suitable for monitoring due to their shared cooling pipe. With two or four SP chains per LLS, all modules were arranged on a single panel without compromising readability. Another restriction was the maximum panel size set by the JCOP framework, which led to a loss of readability if more than one LLS was displayed on a single panel. The legacy code of the monitoring panels as well as mine only use the alias of the depicted LLS as input. All panels depicted in this bachelor thesis display only dummy variables.

In order to simplify monitoring, a single-module temperature and voltage difference display has a corresponding colour background. The temperature spectrum spans from blue for cold, through green for moderate temperatures, to red for hot, as one can see in Fig. 7.1 (left). The optimal voltage value is indicated in white, while pinker fields represent values further away, as one can see in Fig. 7.1 (right).

Figure 7.1: Colour spectra for the colour coding of the temperature values, with blue corresponding to the lowest value of the range and red for the highest, on the left and the voltage values, with white corresponding to the optimal value and pink for the extrema of the range, on the right.

In addition to the individual module temperature and voltage difference values, the displayed information also includes the identifying details of the LLS chain, the name of each module, the grouping of modules within the same SP chain, the placement and direction of the cooling pipe, the modules used as inputs for the interlock, the minimum and maximum values corresponding to the spectral ranges, and the orientation of the modules (whether they are front-facing or back-facing) within the half rings.

The first type of LLS in the OB demonstrator comprises longerons. In the final ITk pixel OB, each longeron has four SP chains: two central chains near the interaction point with six modules each and two outer chains with 12 modules each. The proposed design is

illustrated in Fig. 4.8. The longeron monitoring panel of layer 3 is shown in Fig. 7.2. Due
to the panel size constraints, the C-side of the longeron is positioned above the A-side,
allowing for larger module panels that are necessary for readability. Arrows along the pipe
indicate the placement and direction of the cooling pipe. The legend in the left middle of
the panel identifies the specific longerons displayed and shows how interlock modules are
marked. The temperature and voltage values corresponding to the spectral extremes are
located in the middle right corner of the panel. Modules connected in a single SP chain
are enclosed in a light gray rectangle, whereas interlock modules are highlighted with a
black lattice pattern. Each module's name is displayed vertically on the left side of its
box, with monitoring values stacked next to it. Hovering over a module reveals the names
and aliases of the corresponding data points in text fields. The colour coding of different
labels effectively highlight problematic monitored values.

Figure 7.2: Previous monitoring panel of a layer 2 longeron

The half rings represent the second type of LLS in the OB of the ITk pixel detector. Each
inclined half ring contains two SP chains with 8, 11, or 14 modules per chain, depending
on their placement in layers 2, 3, or 4. Additionally, the half rings are positioned at
either the top or bottom of the detector. Their design is illustrated in Fig. 4.9. The
monitoring panel should clearly indicate the combination of the layer and top/bottom
positions for the current panel. All half ring monitoring panels include a legend with
identifying information, placement and direction of the cooling pipes, a guide for the
values corresponding to the extremes of the colour spectra, gray areas indicating the SP
chains, and an indication of which modules are backward-facing or used as inputs for

the interlock. A panel depicting the layer 2 top half ring on the C-side can be seen in Fig. 7.3. Unlike longerons, the form of the half rings varies with the three different sizes and the presence of both top and bottom half rings. The cooling pipe's direction is counterclockwise from the interaction point, which is determined by the placement of the interlock module.
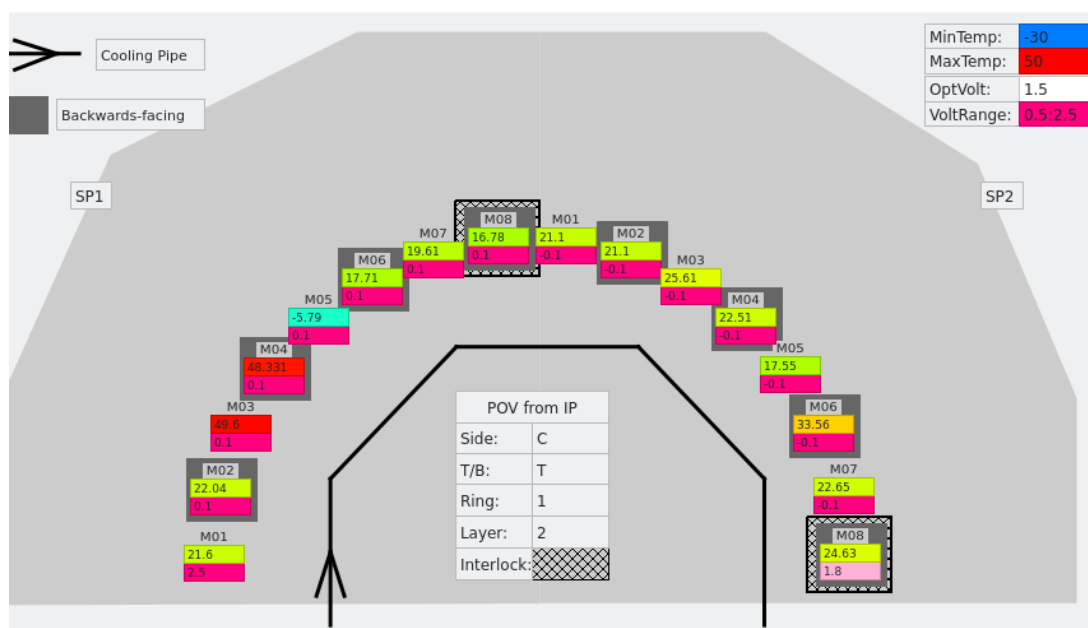

Figure 7.3: Previous monitoring panel of a top layer 2 half ring on the C-side

7.2 Improvements to the Monitoring Software

The primary objective of the panel improvements was to achieve a higher density of information while maintaining a streamlined design that avoids oversaturation of information for the user. In addition, the TFM, discussed in Chapter 6, should be displayed for specialized use cases. Upgrading from CentOS7 to Alma Linux increased the JCOP panel size, providing greater design flexibility.

7.2.1 Changes to the Half Ring Control Panels

With these objectives in mind, I added a colour map as well as a label for the pipe temperature in the half ring, as shown in 7.4. Additionally, a toggle was implemented to the half ring panel, enabling the user to switch between displaying the absolute voltage, as shown in the quick test depicted in Fig. 7.4, and the voltage difference, as shown in the quick test depicted in Fig. 7.5. Due to the modules being powered through serial powering, the voltage difference is the most critical indicator of power consumption for each individual module. However, the absolute voltage remains important for assessing the overall power consumption of the entire SP chain. If the module receives a deviating voltage in the series, this deviation will still be displayed, even if the consumption is correct. Consequently, errors will be inaccurately reflected in the absolute value, especially if the value is colour-coded based on its deviation from the target value. Therefore, the decision was made to only colour-code the voltage difference.
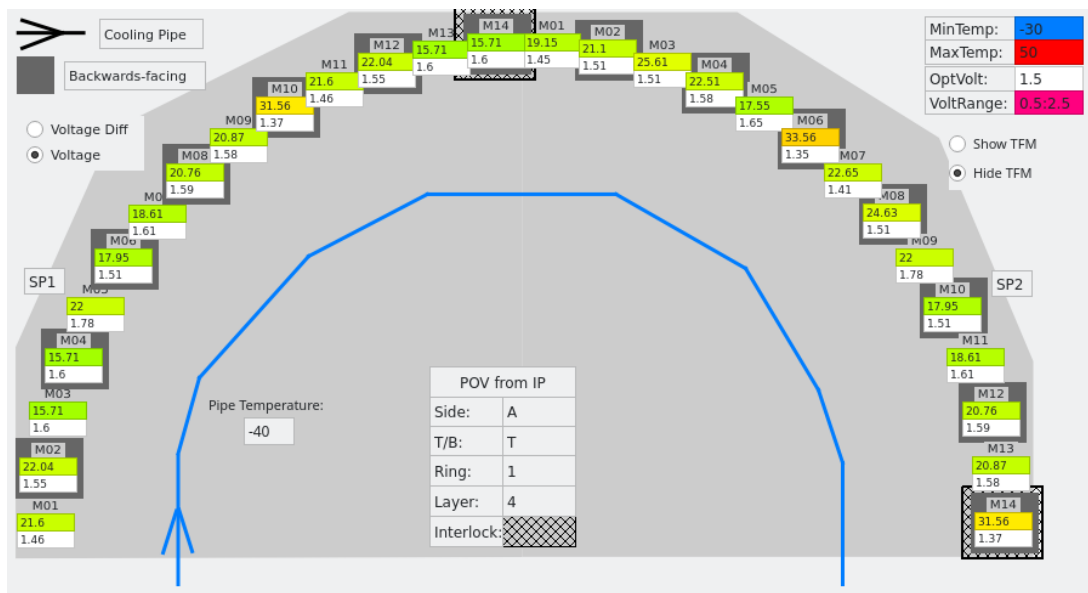

Figure 7.4: Monitoring panel of a top layer 4 half ring on the A-side displaying the temperature and the voltage
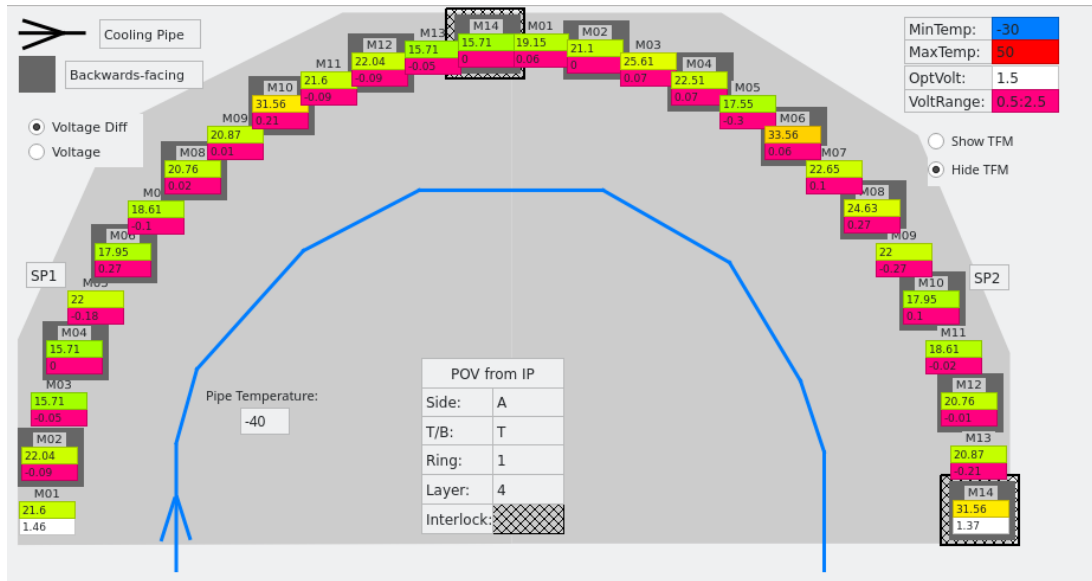
Figure 7.5: Quick test of the monitoring panel of a top layer 4 half ring on the A-side displaying the temperature and the voltage difference

Additionally, a toggle was added to disable, as shown in Fig. 7.4, or enable, as shown in Fig. 7.6, the display of the TFM (introduced in Chapter 6) in a separate label that is initialized using the iteration of the legacy code.
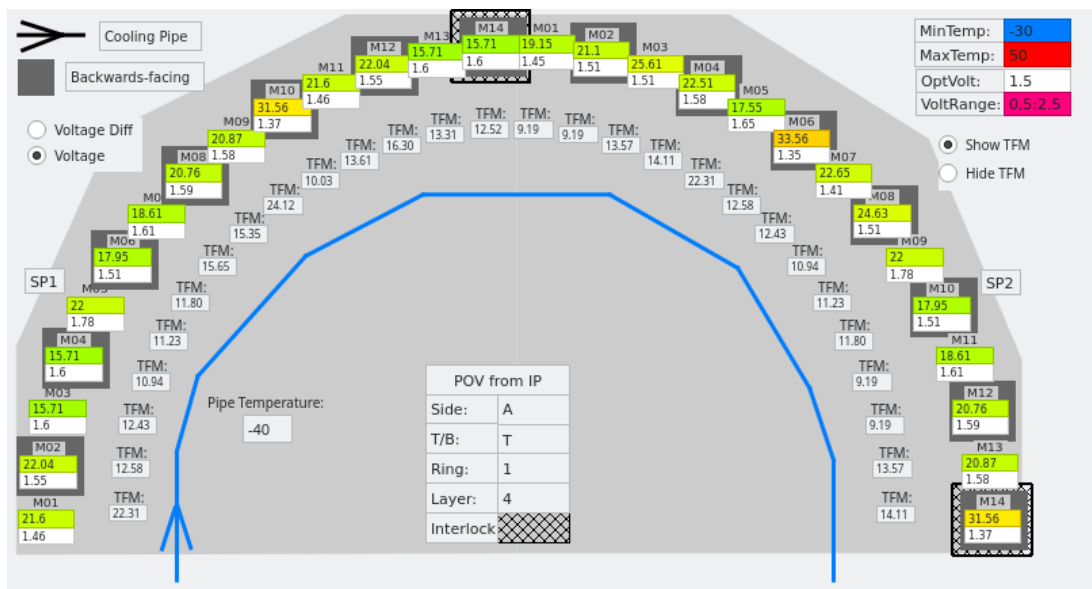

Figure 7.6: Quick test of the monitoring panel of a top layer 4 half ring on the A-side displaying the temperature, voltage difference and the TFM

7.2.2 Suggested Template Changes for the Module Panel

Suggested changes in the scope of system tests involved the modifications of the module template. The display should now show temperature, absolute voltage, voltage difference, and power all at once. Due to the series connection of the modules, the power consumption $P = I \cdot U$ for each module will depend on the voltage difference to the neighbouring module and the current, which remains the same for all elements in the series chain. Incorporating an SP Chain position indicator in the upper left corner, a voltage group indicator in the upper right corner, and a colour mapping for the upper corner labels reflecting the low voltage state (left) and the high voltage state (right) was suggested. The rectangle representing the interlocking module should have a thick border, the modules should have a more detailed name and the entire module, except for the upper corner labels, should be colour-coded instead of colour-coding separate labels. The cumulative changes are depicted in Fig. 7.7.
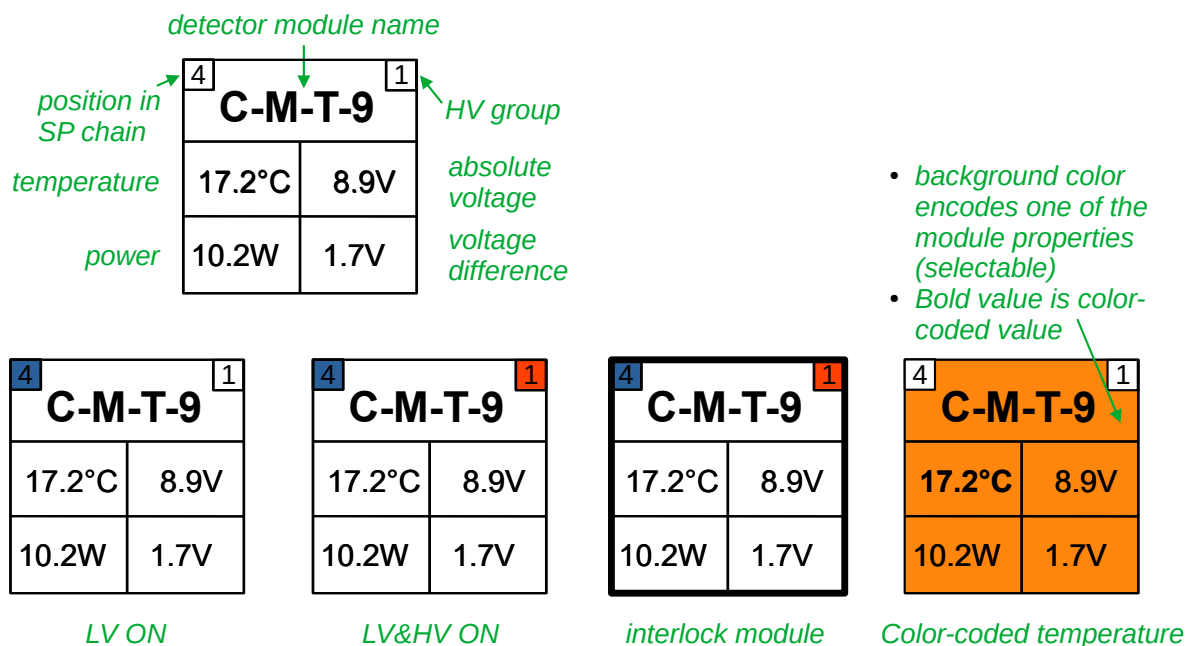

Figure 7.7: Proposed modifications to the module template including enhanced quantity displays, a new name, voltage state indicators in the corners, SP chain position, HV group identification, redesigned interlocks, and updated colour mapping.

7.2.3 Changes to the Longeron Control Panels

To extend the flexibility and usability of the control interface, several modifications were applied to the longeron control panels. Including the implementation of the suggested template. Most aspects of the template were successfully incorporated, as shown in the quick test in Fig. 7.8, while preserving former features, such as the hovering over a module and each separate quantities that leads to the names and aliases of the corresponding data points being displayed. A noteworthy work in progress is the indicator of the high voltage group, for which a function still has to be defined to find the corresponding high voltage group of a given alias using a lookup table. Additionally, it is important to note that the module designation is not correct yet. For that, specific data point aliases must still be defined, a task that will be completed outside the scope of this thesis.

As shown in Fig. 7.8 each module is entirely colour-coded according to the toggle that the user sets, in this case the colour coding of the temperature is selected which uses the colour range of Fig. 7.1 (left). Additional options for the user are the colour coding of power displayed in Fig. 7.9 and voltage difference displayed in Fig. 7.10 according to the colour range of Fig. 7.1 (right).

Figure 7.8: Quick test of the monitoring panel for a layer 3 longeron using the new module template, with the colour mapping toggle set to temperature.

Figure 7.9: Quick test of the monitoring panel for a layer 3 longeron using the new module template, with the colour mapping toggle set to power.

Figure 7.10: Quick test of the monitoring panel for a layer 3 longeron using the new module template, with the colour mapping toggle set to voltage differences.

In addition, seamless communication with a locally run FSM, which is a clone that is

expected to behave like the final project's FSM, is evident in both the quick test shown in Fig. 7.8 and the final user interface (UI) displayed in Fig. 7.11. Because of the current, low voltage and high voltage states of the FSM are indicated in the corners of the module by their respective state colours.

Communication with a locally run FSM, similar to the final project's FSM, works seamlessly with the current code. The evidence for that can be seen in both the quick test shown in Fig. 7.8 and the final user interface (UI) displayed in Fig. 7.11. The current low and high voltage states of the FSM are clearly indicated in the corners of the module by their respective state colours. Furthermore, it is important to note that the dimensions of the monitor panels seem to be well-suited to the designated area in the UI, while also allowing space for future development.
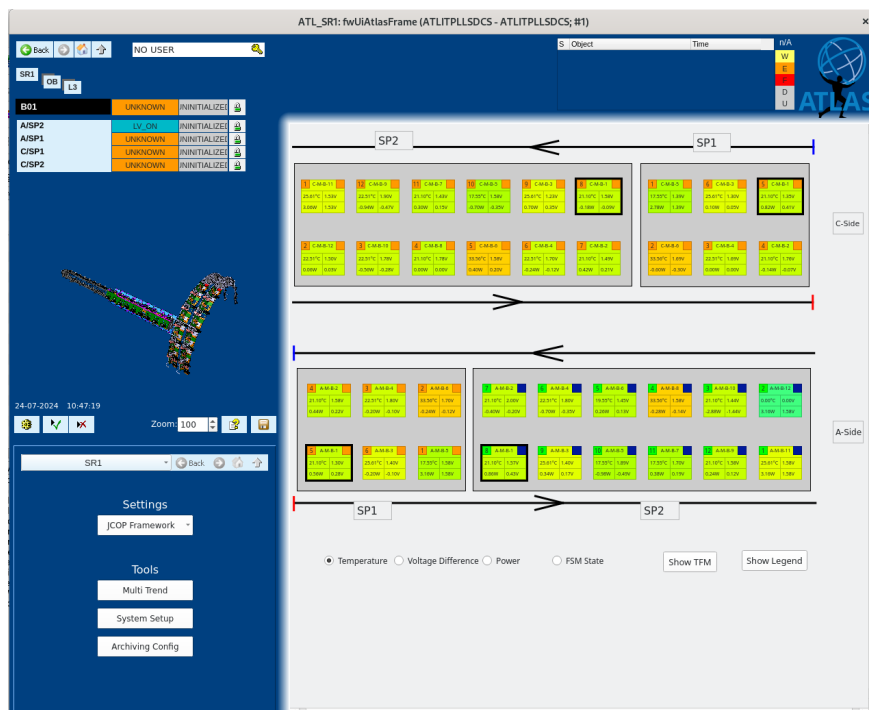

Figure 7.11: The monitoring panel for a layer 3 longeron using the new module template and being displayed in the UI with the locally run FSM

To provide user access to the TFM, I implemented a pop-up window. This design choice streamlines the main panel, acknowledging that the TFM is a critical metric for only a limited number of specialized users. Consequently, it should not occupy excessive space in the standard display. When the user clicks on the "Show TFM" button in the UI, shown in Fig. 7.11, the TFM pop-up window will be depicted by the UI as shown in Fig. 7.12 giving the user an overview over all the modules and their corresponding TFM in form of a table.
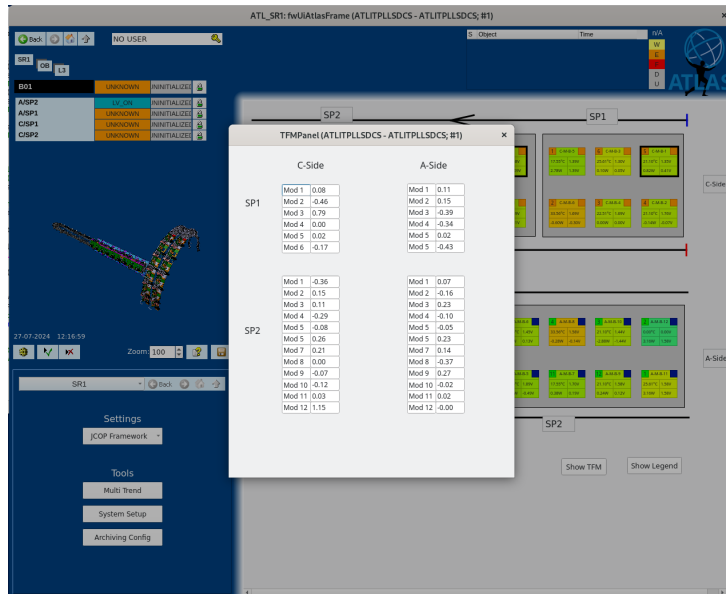
Figure 7.12: The TFM pop-up window being displayed in the UI with the locally run FSM

A further noteworthy change is the replacement of every legend formerly depicted on the panel itself with a pop-up window. When the user clicks on the "Show Legend" button in the UI, shown in Fig. 7.11 the TFM pop-up window will be depicted by the UI as shown in Fig. 7.13. Right now, there is only the colour ranges for each colour map depicted in the legend, but the pop-up still leaves room for further information.
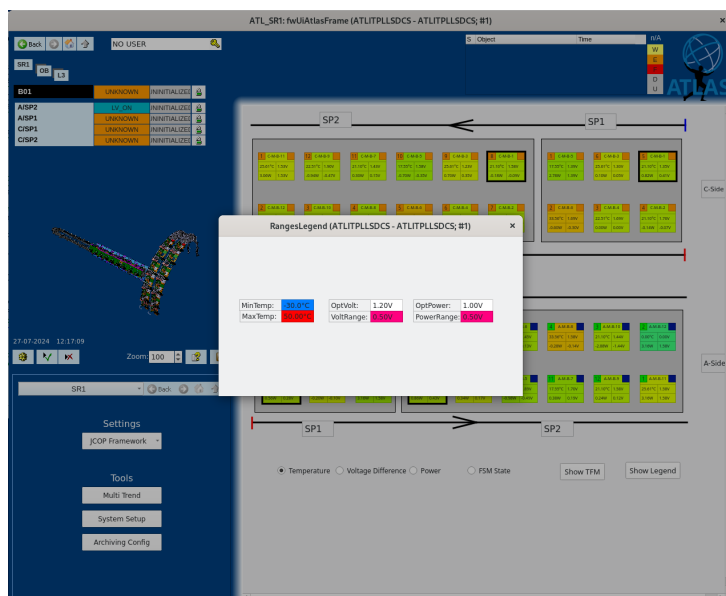

Figure 7.13: The legend pop-up window being displayed in the UI with the locally run FSM

7.2.4 Segmentation of the Loaded Local Support Panel

Finally, I segmented the initialization code of the monitor panel to enable broader use within the UI. The updated code specifically initializes the four SP chains as reference panels, utilizing a dynamic string to convey the necessary information to each one, in order to construct the final depiction of the LLS. The key advantage of this approach is that the code can now be reused in other parts of the UI as a more graphically intuitive monitoring tool by simply calling the individual SP chains as main panels, with the required information passed as a dynamic string. An example use case is marked in the UI in Fig. 7.14, where currently only the temperature and voltage difference of the selected SP chains modules are depicted.
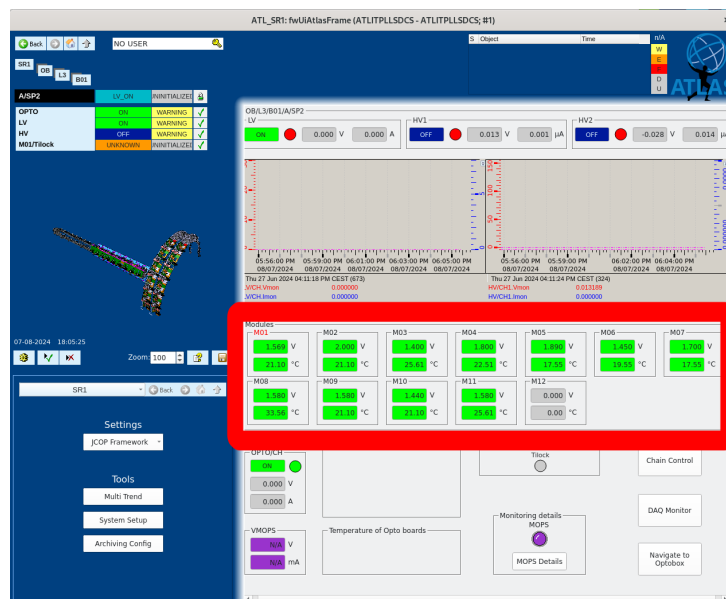

Figure 7.14: An indicated section in the UI that could display a segmented part of the monitoring panel

8 Conclusion and Outlook

8.1 Conclusion

The ITk Pixel Outer Barrel (OB) demonstrator has been successfully completed, along with the Final Design Review (FDR) report. This report include system tests designed to validate the demonstrator setup. Following the FDR, the next phase is the Production Readiness Review (PRR). During the PRR, the involved institutes need to demonstrate their capability to manufacture the components with the specified requirements. This is achieved by constructing prototypes and rigorously testing them. Upon passing the PRR, full-scale production commences.

The Detector Control System (DCS) is currently being optimized under real-world conditions to ensure reliable performance. A fully operational DCS is critical to maximizing the potential of the new detector within the context of the High-Luminosity Large Hadron Collider (HL-LHC) upgrade. The primary objective of this Bachelor's thesis is to enhance the user-friendliness of the DCS for operators and expand the display of useful quantities for the non-expert user. These improvements are expected to significantly reduce operational errors in the ATLAS experiment during the HL-LHC upgrade by simplifying processes and increasing precision.

During my bachelor's thesis, I familiarized myself with the DCS of the ITk pixel OB demonstrator and gained extensive experience with the pre-existing WinCC OA software. I spent a significant amount of time exploring various features and possibilities of WinCC OA. Each design decision was made with respect to the technical possibilities and the demands placed on the graphical user interface.

The first contribution that I made was the implementation of a toggle in the half ring interface, allowing users to switch between displaying the voltage difference and the absolute voltage. I also added a toggle to enable or disable the display of the TFM for a more specialized monitoring. To enhance clarity, I colour-coded the cooling pipes based on temperature and included a small label to display the precise temperature value.

In the longerons, I adopted an entirely different template for the module. With this template, the modules now display not only temperature and voltage difference but also

power and absolute voltage, all at once. Additionally, the low and high voltage states are indicated in the upper corners by their colour, and the SP chain position is shown in the upper left corner. I also improved the user experience by enabling the user to highlight the whole module with the colour map of the power, the voltage difference or the temperature. Furthermore, I implemented two pop-up windows: one for displaying the TFM in a table format and another for showing all the legends that I removed to avoid overstimulation of the user. Lastly, I segmented the initialization code to facilitate further use of the SP chains demonstration in the user interface.

8.2 Outlook

Due to the time constraints of a bachelor's thesis, there were some changes that could not be made. These remain as potential areas for further research.

In the longerons, the high voltage group in the upper right corner has not yet been implemented. Defining a function that uses a lookup table to identify the corresponding high voltage group for a given alias is required for that. Additionally, the data points for the module designation still have to be defined. Further improvements could include integrating additional information into the legend pop-up, enabling dynamic adjustment of colour ranges within the UI via this pop-up and adding another module colour map to indicate the combined state of the FSM. The modules of the half ring are planned to be rewritten in the new template. Additionally, after segmenting the SP chain code, they are planned to be incorporated in as a graphically intuitive monitoring tool in the panels focussing on the SP chains.

Bibliography

[1] L. Evans and P. Bryant, *LHC Machine*, J. Instrum. **3** (2008) S08001 (cit. on p. 1).

[2] M. Thomson, *Modern Particle Physics*, Cambridge University Press, 2013
(cit. on pp. 1, 3–5).

[3] S. L. Glashow, *Partial-symmetries of weak interactions*,
Nucl. Phys. **22** (1961) 579, ISSN: 0029-5582 (cit. on p. 1).

[4] S. Weinberg, *A Model of Leptons*, Phys. Rev. Lett. **19** (1967) 1264 (cit. on p. 1).

[5] A. Salam, *Weak and electromagnetic interactions*,
Conf. Proc. C **680519** (1968) 367 (cit. on p. 1).

[6] A. D. Sakharov,
Violation of CP invariance, C asymmetry, and baryon asymmetry of the universe,
Sov. Phys. Uspekhi **34** (1991) 392 (cit. on p. 1).

[7] F. Zwicky, *Die Rotverschiebung von extragalaktischen Nebeln*,
Helv. Phys. Acta **6** (1933) 110 (cit. on p. 1).

[8] CMS Collaboration, *Observation of a new boson at a mass of 125 GeV with the
CMS experiment at the LHC*, Phys. Lett. B **716** (2012) 30, ISSN: 0370-2693
(cit. on p. 2).

[9] Atlas Collaboration, *Observation of a new particle in the search for the Standard
Model Higgs boson with the ATLAS detector at the LHC*,
Phys. Lett. B **716** (2012) 1, ISSN: 0370-2693 (cit. on p. 2).

[10] Cern, *High Luminosity LHC Project*, 2022,
URL: https://hilumilhc.web.cern.ch (visited on 04/21/2024)
(cit. on pp. 2, 25).

[11] M. Tanabashi et al., *Review of Particle Physics*, Phys. Rev. D **98** (3 2018) 030001
(cit. on pp. 4, 10).

[12] A. Salam, *The Electroweak Force, Grand Unification and Superunification*,
Physica Scripta **20** (1979) 216 (cit. on p. 4).

Bibliography

[13] I. Neutelings, 2017,
      URL: https://tikz.net/axis3d_cms/ (visited on 04/22/2024) (cit. on p. 5).

[14] S. Tavernier, *Experimental Techniques in Nuclear and Particle Physics*,
      Springer Berlin Heidelberg, 2010, ISBN: 978-3-642-00829-0 (cit. on pp. 6, 7, 17).

[15] H. Bethe,
      Zur Theorie des Durchgangs schneller Korpuskularstrahlen durch Materie,
      Annalen der Physik **397** (1930) 325, eprint:
      https://onlinelibrary.wiley.com/doi/pdf/10.1002/andp.19303970303
      (cit. on p. 7).

[16] F. Bloch, *Zur Bremsung rasch bewegter Teilchen beim Durchgang durch Materie*,
      Annalen der Physik **408** (1933) 285, eprint:
      https://onlinelibrary.wiley.com/doi/pdf/10.1002/andp.19334080303
      (cit. on p. 8).

[17] C. Grupen and I. Buvat, *Handbook of Particle Detection and Imaging*,
      Springer Berlin Heidelberg, 2012 (cit. on p. 8).

[18] H. Kolanoski, *Teilchendetektoren*, vol. 1, Springer-Verlag, 2016 921
      (cit. on pp. 9, 14–16, 24).

[19] W. Nakel, *The elementary process of bremsstrahlung*, Phys. Rep. **243** (1994) 317,
      ISSN: 0370-1573 (cit. on p. 9).

[20] R. Gross and A. Marx, *Festkörperphysik*, München: De Gruyter Oldenbourg, 2014,
      ISBN: 9783110358704 (cit. on p. 11).

[21] D. Berney Needleman, *Optical design guidelines for spectral splitting photovoltaic
      systems : a sensitivity analysis approach*, (2014) (cit. on p. 12).

[22] W. Skolaut, *Maschinenbau*, Springer Verlag Berlin, 2015 (cit. on pp. 12, 13).

[23] H. Spieler, *Semiconductor Detector Systems*, Oxford University Press, 2005
      (cit. on pp. 13–15).

[24] O. Brüning, H. Burkhardt, and S. Myers, *The Large Hadron Collider*,
      Prog. Part. Nucl. Phys. **67** (2012) 705, ISSN: 0146-6410 (cit. on p. 19).

[25] E. Lopienska, *The CERN accelerator complex layout in 2022*, 2022,
      URL: https://cds.cern.ch/record/2800984 (visited on 04/21/2024)
      (cit. on p. 20).

[26] ATLAS Collaboration,
The ATLAS Experiment at the CERN Large Hadron Collider,
J. Instrum. **3** (2008) S08003 (cit. on pp. 20, 22–24).

[27] ATLAS Collaboration, *The ATLAS Inner Detector commissioning and calibration*,
Eur. Phys. J. C **70** (2010) 787 (cit. on p. 22).

[28] I. Perić et al., *The FEI3 readout chip for the ATLAS pixel detector*,
Nuclear Instruments and Methods in Physics Research Section A: Accelerators,
Spectrometers, Detectors and Associated Equipment **565** (2006) 178, Proceedings
of the International Workshop on Semiconductor Pixel Detectors for Particles and
Imaging, ISSN: 0168-9002 (cit. on p. 22).

[29] A. L. Rosa and on behalf of ATLAS collaboration,
The ATLAS Insertable B-Layer: from construction to operation,
J. Instrum. **11** (2016) C12036 (cit. on p. 23).

[30] M. Garcia-Sciveres et al., *The FE-I4 pixel readout integrated circuit*,
Nucl. Inst. and Meth. **636** (2011) S155, ISSN: 0168-9002 (cit. on p. 23).

[31] A. Ahmad et al.,
The silicon microstrip sensors of the ATLAS semiconductor tracker,
Nucl. Instrum. Methods Phys. Res. **578** (2007) 98, ISSN: 0168-9002
(cit. on pp. 23, 24).

[32] Atlas Collaboration, *ATLAS Phase-II Upgrade Scoping Document*,
tech. rep. CERN-LHCC-2015-020, LHCC-G-166, CERN, 2015 (cit. on p. 26).

[33] ATLAS Collaboration, *Expected tracking and related performance with the updated
ATLAS Inner Tracker layout at the High-Luminosity LHC*,
tech. rep. ATL-PHYS-PUB-2021-024, CERN, 2021 (cit. on pp. 26, 27).

[34] D. Giugni et al.,
Design Overview of the Bare Local Supports for the ITk Pixel Outer Barrel,
tech. rep. AT2-IP-ER-0013, ATLAS Collaboration, 2021 (cit. on p. 27).

[35] D. A. Feito et al., *On-Detector Services - Outer Barrel, ITk Pixel - Supporting
documentation for PDR*, 2020, URL: https://indico.cern.ch/event/881276/
(cit. on p. 27).

[36] J. Francisca and M. Sánchez, *ATLAS ITk Pixel Detector Overview*,
J. Phys.: Conference Series **2374** (2022) 012061 (cit. on p. 28).

[37] M. Garcia-Sciveres, *The RD53A Integrated Circuit*,
tech. rep. CERN-RD53-PUB-17-001, CERN, 2017 (cit. on p. 28).

Bibliography

[38] RD53 Collaboration, *RD53B users guide*, tech. rep. CERN-RD53-PUB-21-001, CERN, 2020 (cit. on p. 28).

[39] A. B. Poy et al., *The detector control system of the ATLAS experiment*, J. Instrum. **3** (2008) P05006 (cit. on pp. 29, 30, 35).

[40] O. Holme, M. González-Berges, P. Golonka, and S. Schmeling, *The JCOP Framework*, tech. rep. CERN-OPEN-2005-027, CERN, 2005 (cit. on p. 29).

[41] T. Henss et al., *The hardware of the ATLAS Pixel Detector Control System*, J. Instrum. **2** (2007) P05006 (cit. on p. 30).

[42] S. Schäpe, *ITk SR1 CO2 Cooling Plant for Pixel*, 2019, URL: `https://twiki.cern.ch/twiki/pub/Atlas/ITkSR1CO2PlantPixeloperation/SR1_CO2_system_test.pdf` (cit. on p. 31).

[43] G. Schnell and B. Wiedemann, *Bussysteme in der Automatisierungs- und Prozesstechnik*, Springer Fachmedien Wiesbaden, 2019 (cit. on p. 31).

[44] W. Mahnke, S.-H. Leitner, and M. Damm, *OPC Unified Architecture*, Springer Berlin Heidelberg, 2009 (cit. on p. 31).

[45] P. Nikiel et al., *OPC Unified Architecture within the Control System of the ATLAS Experiment*, (2014) (cit. on p. 31).

[46] P. P. Nikiel, B. Farnham, V. Filimonov, and S. Schlenker, *Generic OPC UA Server Framework*, J. Phys. Conf. Ser. **664** (2015) 082039 (cit. on p. 32).

[47] ed. by B. Farnham, *Wiener OPC-UA User Manual*, JCOP project (2021), version 1.2.0, eprint: `https://edms.cern.ch/ui/file/2169631/1.2.0/Wiener_OPCUA_Server_User_Manual.pdf` (cit. on p. 32).

[48] *WinCC OA Architecture*, URL: `https://www.winccoa.com/documentation/WinCCOA/3.18/en_US/GettingStarted/GettingStarted-06.html` (visited on 04/25/2024) (cit. on p. 33).

[49] J. H. Conway, *Regular Algebra and Finite Machines*, Dover Publications, 2012, ISBN: 978-0-486-48583-6 (cit. on p. 34).

[50] R. Kopeliansky and S. Schlenker, *DCS: Requirements Document for HL-LHC*, tech. rep. ATU-GE-ES-0004, ATLAS Collaboration, 2020 (cit. on p. 35).

[51] R. Ahmad, M. Karagounis, S. Kersten, N. Lehmann, and C. Zeitnitz,
Specification for the Pixel DCS ASIC: Monitoring Of Pixel System,
tech. rep. AT2-IP-ES-0001, 2021 (cit. on p. 35).

[52] C. Gemme et al., *ITk Interlock System Strategy*, tech. rep. AT2-IE-ES-0005,
ATLAS Collaboration, 2021 (cit. on p. 36).

[53] M. Ressegotti, *ITk Pixel DCS*, 2022,
URL: https://twiki.cern.ch/twiki/bin/%20viewauth/Atlas/ITkPixelDCS
(cit. on p. 36).

[54] G. Beck and G. Viehhauser,
Analytic model of thermal runaway in silicon detectors,
Nucl. Instrum. Methods Phys. Res. A **618** (2010) 131, ISSN: 0168-9002
(cit. on p. 37).

[55] M. Moll, *Radiation damage in silicon particle detectors: Microscopic defects and
macroscopic properties*, Dissertation: Universität Hamburg, 1999 (cit. on p. 37).

[56] M. Tavlet and H. Van der Burgt, *Radiation resistance and other safety aspects of
high-performance plastics by ERTA*, tech. rep. CERN-TIS-94-13, CERN, 1994
(cit. on p. 37).

[57] F. M. Sanchez, *Carbon Based Local Supports for the ATLAS ITk Pixel Detector,*
PoS Proc. Sci. (2023) (cit. on pp. 38–40).

[58] *Technical Design Report for the ATLAS Inner Tracker Pixel Detector,*
tech. rep. CERN-LHCC-2017-021, ATLAS-TDR-030, CERN, 2017 (cit. on p. 41).

[59] A. Gaa, *Development of the Detector Control System of the ITk Outer Barrel
Demonstrator for the ATLAS Experiment,*
URL: https://www.uni-goettingen.de/de/550897.html,
II.Physik-UniGö-MSc-2022/07, 2022 (cit. on p. 42).

Acknowledgment

First and foremost, I extend my sincere gratitude to Prof. Dr. Stan Lai for granting me the opportunity to complete my Bachelor's thesis within his research group. The weekly research discussions and group meetings were instrumental in advancing my work and provided valuable insights. I am also grateful to apl. Prof. Dr. Jörn Große Knetter for serving as my second examiner.

I owe a special thanks to Anne Gaa, who generously answered my questions at any time, despite her own demanding schedule. Her support was crucial, especially in respect to the understanding of her code. Additionally, I would like to thank Hans Jooß for always being willing to assist me with all my problems, especially concerning the FSM.

Lastly, I would like to express my deepest appreciation to my parents, siblings and my girlfriend for their unwavering support.

Erklärung nach §13(9) der Prüfungsordnung für den Bachelor-Studiengang Physik und den Master-Studiengang Physik an der Universität Göttingen: Hiermit erkläre ich, dass ich diese Abschlussarbeit selbständig verfasst habe, keine anderen als die angegebenen Quellen und Hilfsmittel benutzt habe und alle Stellen, die wörtlich oder sinngemäß aus veröffentlichten Schriften entnommen wurden, als solche kenntlich gemacht habe.

Darüberhinaus erkläre ich, dass diese Abschlussarbeit nicht, auch nicht auszugsweise, im Rahmen einer nichtbestandenen Prüfung an dieser oder einer anderen Hochschule eingereicht wurde.

Göttingen, den 18. November 2024

(Manuel Riedemann)